Journal of Nuclear Materials 630 (2026) 156750

Contents lists available at ScienceDirect

Journal of Nuclear Materials

journal homepage: www.elsevier.com/locate/jnucmat

Creep-Fatigue Design of RAFM Steels Using Physics-Informed and Data-Driven Surrogate Models with Multi-Objective Optimisation

Pengxin Wang [a,b], Yian Lin [a], Mingda Tian [a], G.M.A.M. El-Fallah [a,*]

[a] School of Engineering, University of Leicester, Leicester LE1 7RH, UK
[b] Nanjing Iron & Steel United Co., Ltd., Nanjing, 210035, Jiangsu, China

HIGHLIGHT

- Dual-mechanism PINN and MLP surrogates achieve high-fidelity creep and LCF prediction.
- SHAP analysis recovers governing physics across stress-, diffusion- and cyclic regimes.
- Cr–W–Ta interactions show strong synergy at low T and degradation-driven behaviour at high T.
- Surrogates enable NSGA-II optimisation of RAFM compositions for balanced creep–fatigue life.
- Optimised alloys surpass Eurofer97, reaching $2.5 - 5.1 \times 10^3$h creep life and $\log_{10}N_f \approx 3.85 - 4.18$.

GRAPHICAL ABSTRACT

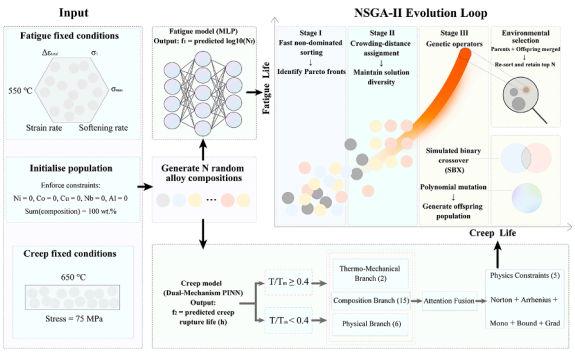

ARTICLE INFO

Keywords:
Reduced-activation ferritic-martensitic (RAFM) steels
Creep rupture
Low-cycle fatigue (LCF)
Physics-informed neural networks (PINNs)
Multi-objective optimisation
NSGA-II

ABSTRACT

Designing reduced-activation ferritic-martensitic (RAFM) steels capable of simultaneously resisting creep deformation and low-cycle fatigue (LCF) damage is a key requirement for structural materials in future fusion demonstration reactors (DEMO), where components are exposed to elevated temperatures and cyclic loading. However, achieving balanced creep-fatigue performance remains challenging because the mechanisms governing long-term creep rupture and cyclic plasticity are fundamentally different and often conflicting. In this study, two complementary surrogate models are developed to address this creep-fatigue design challenge: a dual-mechanism physics-informed neural networks (PINNs) for predicting creep rupture behaviour and a multi-layer perceptron (MLP) model for LCF performance. The models are trained on consolidated datasets including experimental creep rupture data, cyclic fatigue properties, alloy compositions and thermophysical descriptors. The creep PINN achieves $R^2 = 0.96$ and captures the transition from stress-controlled dislocation creep at lower homologous temperatures ($T/T_m < 0.4$, where T_m represents the alloy melting temperature) to diffusion-dominated behaviour at higher temperatures ($T/T_m \geq 0.4$), corresponding approximately to 500-600°C for typical RAFM steels, while the fatigue MLP attains $R^2 = 0.97$. Model interpretability based on SHAP (SHapley Additive exPlanations) reveals temperature-dependent shifts in creep kinetics and identifies the total strain range ($\Delta\varepsilon_{total}$), temperature and Cr-W-Ta alloying interactions associated with precipitation strengthening as key factors influencing LCF behaviour. Feature interaction analysis based on SHAP interaction values further indicates cooperative Cr-W-Ta strengthening at lower temperatures and degradation-dominated behaviour at

* Corresponding author.
E-mail address: gmae2@leicester.ac.uk (G.M.A.M. El-Fallah).

https://doi.org/10.1016/j.jnucmat.2026.156750
Received 24 January 2026; Received in revised form 28 April 2026; Accepted 18 May 2026
Available online 21 May 2026

higher temperatures. Integrating both surrogate models into a multi-objective optimisation framework based on Non-dominated Sorting Genetic Algorithm II (NSGA-II) generated a Pareto front of alloy compositions with improved predicted creep rupture life and fatigue life compared with Eurofer97, achieving $\log_{10}N_f = 3.85$-4.18 and predicted creep rupture time of 2.5-5.1 $\times 10^3$ h at 650°C. These results demonstrate an interpretable framework for the creep-fatigue-informed design of RAFM steels under fusion-relevant operating conditions.

Nomenclature

A	Pre-exponential constant in Arrhenius-type creep law
Q	Activation energy for creep ($J{\cdot}mol^{-1}$)
R	Universal gas constant ($J{\cdot}mol^{-1}K^{-1}$)
D_{eff}	Effective diffusion coefficient ($m^2{\cdot}s^{-1}$)
$\Delta\delta$	Atomic size mismatch
ΔS_{mix}	Configurational (mixing) entropy
VEC	Valence electron concentration
σ	Applied stress in creep tests (MPa)
σ_1	Initial stress in LCF hysteresis loop (MPa)
$\sigma_{\max}$	Peak stress in LCF hysteresis loop (MPa)
σ/T	Stress-to-temperature ratio
T	Absolute temperature (K)
T/T_{m}	Homologous temperature (normalised temperature ratio)
$\Delta\varepsilon_{\text{total}}$	Total strain range in LCF tests (%)
L_{bound}	Boundary regularisation loss term
L_{data}	Data-fidelity loss term (mean-squared error between prediction and experiment)
L_{grads}	Gradient-smoothness regularisation loss term
L_{mono}	Monotonicity loss term enforcing physically correct trends
L_{soft}	Soft-physics loss term based on Arrhenius creep prior
L_{total}	Total loss function of the creep PINN
f_1	Feature embedding extracted from the loading-condition branch ($\sigma - T$ domain)
f_2	Feature embedding extracted from the composition branch
f_3	Feature embedding extracted from the thermo-physical descriptor branch ($\Delta\delta$, ΔS_{mix}, VEC, D_{eff}, T/T_{m}, σ/T)
α	Attention weight vector assigning the relative importance of each feature domain
W	Learnable projection matrix that maps concatenated features into attention logits
f_{fused}	Final fused latent representation obtained as the weighted combination of the three feature embeddings
$ReLU$	Rectified Linear Unit activation function, defined as $ReLU(x) = max(0, x)$
$\alpha_1 - \alpha_4$	Weighting coefficients of individual physics-based loss terms
λ	Coupling coefficient controlling the contribution of the Arrhenius prior
$\langle\cdot\rangle$	Batch average operator
R^2	Coefficient of determination
$RMSE$	Root-mean-squared error
MAE	Mean absolute error
MSE	Mean squared error
$F(x)$	Vector of objective functions in multi-objective optimisation
$f_1(x), f_2(x)$	Objective functions for creep and fatigue performance
N_f	Fatigue life (number of cycles to failure)
N_f^{Euro}	Experimental fatigue life of Eurofer97 under fixed conditions
t_r	Creep rupture time (h)
t_r^{Euro}	Experimental rupture time of Eurofer97 under fixed conditions (h)
BCC	Body-centred cubic
RAFM	Reduced-activation ferritic-martensitic (steel)
LCF	Low-cycle fatigue
Eurofer97	A 9Cr reduced-activation ferritic-martensitic steel developed in Europe as a reference structural material for fusion blanket applications, taken as the baseline alloy in this work
CLAM	China Low Activation Martensitic steel
DBTT	Ductile-to-brittle transition temperature
DEMO	Demonstration fusion power plant
HEA	High-entropy alloy
IN-RAFM	India-specific reduced-activation ferritic-martensitic steel
JLF-1	Japanese Low-activation Ferritic steel grade 1
MLP	Multilayer perceptron
NSGA-II	Non-dominated Sorting Genetic Algorithm II
PINNs	Physics-informed neural networks
RF	Random forest
GBDT	Gradient-boosted decision trees
SHAP	SHapley Additive exPlanations
XGBoost	eXtreme Gradient Boosting

1. Introduction

Reduced-activation ferritic-martensitic (RAFM) steels represent one of the most promising structural materials for advanced nuclear systems, including fusion blanket systems, accelerator-driven systems, and Generation IV fission reactors [1,2]. Their advantages arise from the tempered martensitic microstructure that provides a favourable balance between high-temperature strength, radiation damage resistance and low long-term radioactivation, making RAFM steels such as Eurofer97 the current reference materials for Fusion DEMO blanket concepts [3–6]. Despite these advantages, the structural lifetime of RAFM steels is largely governed by two thermomechanical degradation mechanisms. High-temperature creep governs the accumulation of damage during prolonged exposure to elevated temperatures [7], whereas LCF arises from cyclic thermomechanical loading that produces repeated plastic strain. In RAFM steels, LCF typically occurs under strain-controlled conditions with total strain ranges of approximately 0.3-1.0 % and fatigue lives ranging from 10^3 to 10^5 cycles, depending on the temperature and strain amplitude [8–10]. Creep and LCF effects play central roles in determining the operational design window of RAFM steels. In fusion reactor blanket structures, RAFM steels are typically expected to operate within an intermediate temperature window of approximately 300-650°C, where structural components are subjected to sustained mechanical stresses arising from internal pressure, thermal gradients and structural constraints [11]. Typical design stresses are on the order of tens to over one hundred megapascals, depending on the component geometry and loading conditions. Under such conditions, the upper operating temperature limit is largely constrained by thermal creep deformation, while cyclic thermomechanical loading can simultaneously induce low-cycle fatigue damage. Furthermore, as components are often subjected to simultaneous or sequential creep-fatigue interactions [12,13], the concurrent optimisation of both properties has

become essential for ensuring the reliable operation of fusion systems over extended service periods.

Creep deformation in RAFM steels is controlled by a complex interplay between solid-solution strengthening, subgrain evolution, dislocation recovery kinetics and the behaviour of Laves phase, $M_{23}C_6$ carbides and MX precipitates [7,14]. Alloying elements such as Cr, W and Ta strongly influence microstructural stability by modifying diffusion pathways, particle coarsening rates and grain boundary pinning [15,16]. Numerous experimental studies on 9-12 Cr and RAFM steels show that even small variations in alloy composition, combined with modest differences in processing history, can lead to significant large changes in creep performance, with rupture lifetimes differing by up to one to two orders of magnitude [17,18]. Similarly, LCF performance results from the interplay between cyclic softening, dynamic strain ageing, dislocation rearrangement and precipitate shearing, all of which are strongly influenced by alloy chemistry [19,20]. Understanding and controlling these mechanisms experimentally is expensive and time-consuming, and the interactions between alloying elements are often nonlinear, strongly coupled, and difficult to predict [21].

In nuclear energy systems, structural materials are also exposed to intense neutron irradiation during service. Irradiation can significantly influence the microstructural stability and deformation behaviour of RAFM steels [1,22]. Neutron irradiation in the typical operating temperature range of approximately 300-650°C has been reported to introduce defect clusters, dislocation loops and solute segregation [23,24], which interact with existing strengthening precipitates such as $M_{23}C_6$ carbides, MX carbonitrides and Laves phases [25–27]. These interactions can modify the distribution, size and number density of precipitates and thereby affect dislocation motion, grain boundary stability and time-dependent deformation mechanisms.

Irradiation temperature and dose are known to play important roles in determining the stability or coarsening behaviour of precipitates, which can influence the microstructural evolution associated with high-temperature deformation and cyclic loading [5,28]. It should be noted, however, that the present study focuses on creep-fatigue behaviour under non-irradiated conditions. The aim of this work is to investigate the coupled creep-fatigue mechanisms and modelling approaches under thermomechanical loading without irradiation. Nevertheless, irradiation remains an important factor for structural materials in nuclear reactor environments and its influence on creep-fatigue behaviour deserves further investigation.

Creep-fatigue interaction is a critical issue for structural materials operating under high-temperature cyclic loading in nuclear energy systems. In ferritic-martensitic steels such as RAFM alloys, the interaction arises from the coupling between cyclic plastic deformation, time-dependent creep strain accumulation, and environmental effects during service. Experimental studies have shown that the microstructure of RAFM steels evolves significantly during creep-fatigue loading. The tempered martensitic structure contains complex boundaries and precipitates that provide strength under service conditions, but cyclic deformation and high-temperature exposure can lead to substructural coarsening and dislocation annihilation, resulting in progressive softening and degradation of mechanical properties [12]. Sequential creep-fatigue experiments further reveal that the interaction behaviour strongly depends on loading history. In particular, fatigue pre-exposure can significantly reduce the remnant creep rupture time due to pronounced cyclic softening, whereas creep pre-exposure has a relatively weaker effect on fatigue life because creep damage develops gradually through microstructural degradation and precipitation processes [29].

Despite extensive studies, the mechanisms governing creep-fatigue interaction remain incompletely understood. One major limitation is that creep-fatigue experiments require very long testing times and complex loading conditions, which restrict the amount of available experimental data. As a result, the interaction behaviour of RAFM steels under different service conditions has not yet been fully clarified. To address these challenges, several modelling approaches have been proposed. One representative approach is mechanism-based lifetime modelling, where creep-fatigue damage is separated into crack initiation and crack propagation stages. For example, Fournier *et al.* [30] developed a predictive model in which crack initiation is described using the Tanaka-Mura model and crack propagation follows the Tomkins formulation.

Another widely used strategy is continuum damage modelling, where creep-fatigue interaction is described using phenomenological damage evolution equations that couple cyclic plasticity and time-dependent creep deformation [31]. Although such models can capture the general trends of creep-fatigue behaviour, they typically require extensive experimental calibration and may not fully represent the complex microstructural mechanisms involved.

Therefore, despite the progress made by both mechanism-based and continuum modelling approaches, predicting creep-fatigue interaction in RAFM steels remains a challenging problem, particularly under limited experimental data conditions.

A schematic overview of the current understanding of creep, low-cycle fatigue (LCF), and their interaction in RAFM steels is presented in Fig. 1. The diagram summarises the key mechanisms governing creep and fatigue behaviour, including diffusion, dislocation climb, and microstructural coarsening during creep, as well as cyclic strain, plastic deformation, and crack nucleation during low-cycle fatigue. It also illustrates the main factors associated with creep-fatigue interaction, including high temperature, sustained stress, and cyclic loading. In addition, the figure highlights the principal features of the combined creep-fatigue damage process, namely microstructural softening and coarsening, oxidation-assisted cracking, accelerated crack growth, and reduced structural lifetime. Finally, commonly used modelling approaches for analysing creep-fatigue interaction are summarised, including mechanism-based models and continuum damage models, together with the current challenges in predicting creep-fatigue behaviour, particularly limited experimental data, the complexity of coupling mechanisms, and poor predictive performance.

In recent years, data-driven models and machine learning (ML) surrogates have emerged as powerful tools for exploring high-dimensional alloy design spaces. Applications in high-entropy alloys, superalloys and steels have demonstrated that ML can capture composition-microstructure-property linkages that are inaccessible to classical regression or CALPHAD-only approaches [32–35]. However, two limitations remain prominent. First, purely statistical models often fail to generalise outside the domain of training data due to the lack of mechanistic constraints [36]. Second, ML models typically target isolated properties, while practical alloy design requires the simultaneous optimisation of multiple, often competing, performance metrics such as creep strength, fatigue resistance, toughness and irradiation tolerance [37]. Multi-objective optimisation methods, including genetic algorithms (GA), Bayesian optimisation and the NSGA-II, have shown significant promise in generating Pareto-optimal compositions, but their success strongly depends on the fidelity of the surrogate models used to evaluate candidate alloys [38–40].

To address these challenges, PINNs have recently attracted increasing attention as a means of embedding mechanistic knowledge directly into machine-learning frameworks. By incorporating constitutive relations, energy-based constraints or kinetic laws, PINNs provide improved extrapolation capability and physical interpretability compared with conventional black-box models [41,42]. Despite this progress, no existing study has integrated a dual-mechanism PINNs for creep with a complementary fatigue life surrogate models to enable a unified optimisation framework for RAFM steels. Although SHAP-based interpretability has been widely applied in materials informatics, its role in validating physics-informed surrogates models and guiding composition-aware optimisation remains largely unexplored.

In this context, the present work develops an integrated creep-fatigue alloy design framework based on two high-fidelity surrogate models: (i) a dual-mechanism physics-informed neural network for predicting creep

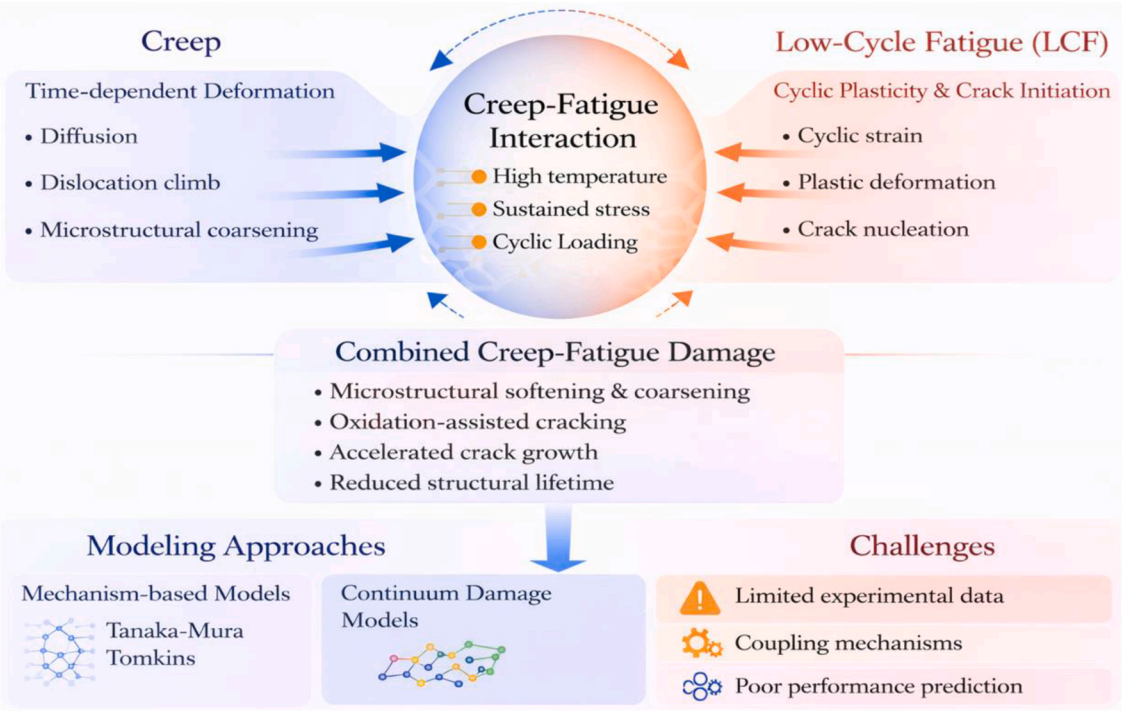

Fig. 1. Schematic overview of creep deformation, low-cycle fatigue (LCF), and their interactions in RAFM steels under high-temperature cyclic loading.

rupture times across low- and high-temperature regimes, and (ii) an MLP-based fatigue life model trained to capture stress evolution, cyclic softening behaviour and strain-dependent LCF responses. Both models incorporate extensive feature engineering, including elemental descriptors, thermodynamic parameters and diffusion-based metrics, and their predictions show strong consistency with previously reported experimental studies on RAFM steels. SHAP analyses further confirm that the learned feature contributions are physically consistent with established strengthening and recovery mechanisms in RAFM steels.

These surrogate models were subsequently embedded in an NSGA-II evolutionary search to enable multi-objective optimisation of alloy composition. The optimisation aims to identify compositions that balance improvements in creep rupture time and LCF resistance under fixed loading conditions. To ensure physical feasibility and nuclear compatibility, high-activation elements (Ni, Co, Nb, Cu, Al) were excluded from the design space, while Fe was treated as the balance element. The resulting Pareto front provides a continuous spectrum of optimal trade-offs between creep and fatigue performance, highlighting compositional pathways that offer balanced strengthening across both deformation regimes.

Overall, this study presents a unified framework that combines physics-informed modelling, interpretable ML and multi-objective evolutionary optimisation to accelerate the design of next-generation RAFM steels. The proposed approach provides a transferable blueprint for developing structural materials that must satisfy multiple competing requirements under extreme service conditions.

2. Methodologies and data overview

2.1. Machine learning models

To model creep rupture and LCF behaviour of RAFM steels, several machine-learning methods with different characteristics were evaluated in this study, including physics-informed neural networks (PINNs), multilayer perceptron (MLP), random forest (RF), gradient-boosted decision trees (GBDT), and Extreme Gradient Boosting (XGBoost). These methods were selected because they offer complementary strengths for the two prediction tasks, rather than to provide a general overview of common algorithms.

The creep problem involves strong nonlinearity, heterogeneous data sources, and clear physical dependence on temperature and stress. This requires not only predictive accuracy but also physically consistent behaviour. In contrast, the LCF task is primarily a nonlinear regression problem governed by alloy composition and cyclic deformation descriptors, where flexibility and stable generalisation are more important. For this reason, different model types were examined based on their suitability for each dataset and task.

PINNs were used mainly for creep prediction because they allow physical constraints to be incorporated into training, helping preserve realistic trends under limited and heterogeneous data conditions. The MLP was applied to LCF prediction due to its ability to capture complex nonlinear relationships between compositional and mechanical features and fatigue life. RF, GBDT, and XGBoost were included as benchmark models, as tree-based ensemble methods often perform well on structured tabular data and provide useful reference points. The following subsections introduce each method with emphasis on its role, strengths, and limitations in this work.

2.1.1. Physics-informed neural network (PINNs)

PINNs were used primarily for creep rupture prediction [43,44], as the problem involves complex composition-processing-property relationships together with a clear dependence on temperature and stress. The model therefore needs to do more than fit the data; it must also reflect the thermally activated nature of high-temperature deformation. This is especially important because the creep dataset was assembled from multiple sources and covers a wide range of alloy compositions, temperatures, stresses, and rupture times.

Purely data-driven models can fit the training data well, but they may behave unrealistically when data are sparse or when predictions approach the limits of the dataset. This is a concern for creep, where rupture life is expected to decrease consistently with increasing temperature and stress, while the governing mechanisms evolve with homologous temperature [45,46]. For this reason, PINNs were considered more suitable than conventional black-box neural networks for this task.

One of the main advantages of PINNs is that prior metallurgical knowledge can be incorporated directly into the loss function. In this work, the model is guided by both experimental data and physically motivated constraints based on creep kinetics and thermomechanical trends. This improves consistency and helps stabilise training across a heterogeneous dataset. It also makes the model more reliable as a surrogate for subsequent optimisation, since unrealistic creep predictions would directly affect alloy design outcomes.

At the same time, applying PINNs is not straightforward. Creep behaviour in RAFM steels cannot be described by a single regime across all conditions, and the balance between data fitting and physical constraints requires careful tuning. If the constraints are too weak, the model behaves like a standard neural network; if too strong, it may lose flexibility and underfit the data. The PINN approach was therefore chosen because it provides a practical balance between accuracy, physical consistency, and reliability for the creep rupture problem considered.

2.1.2. Multilayer perceptron (MLP)

MLP [47,48] was used primarily for predicting LCF life. In contrast to creep rupture, the LCF problem is governed more directly by nonlinear relationships between alloy composition, mechanical descriptors derived from hysteresis behaviour, and fatigue life [19,49]. The dataset does not show the same clear mechanism transitions seen in creep, so explicit physical constraints of that type are not required.

An MLP is well suited to capturing complex interactions among compositional variables, stress-related descriptors, strain range, strain rate, softening behaviour, and temperature. These factors influence cyclic deformation and fatigue life in a strongly coupled way that is difficult to represent using simple analytical models. A flexible nonlinear model is therefore more appropriate, allowing the relationship between inputs and fatigue life to be learned directly from the data without imposing restrictive assumptions.

Another practical reason for using the MLP is its suitability for medium-sized tabular datasets such as the one used in this work. The dataset combines alloy chemistry with mechanically derived features, and the target variable is continuous. Under these conditions, the MLP delivered strong predictive performance while remaining relatively straightforward to train and optimise.

There are, however, some limitations. The model is less interpretable than simpler regression approaches unless additional tools are used, and its performance can depend on architectural choices such as network depth, hidden layer size, and dropout. It also does not enforce physical constraints. In this case, these limitations were acceptable, as the LCF problem was treated as a single-regime nonlinear regression task, and interpretation was supported using SHAP analysis rather than the model structure itself. For these reasons, the MLP was selected as the final model for LCF prediction, providing a good balance between flexibility, stability, and predictive accuracy for the dataset considered.

2.1.3. Random Forest (RF)

RF was included as a benchmark for comparison with the neural-network-based approaches [50,51]. Both the creep and fatigue datasets are tabular and include mixed numerical descriptors, making RF a useful reference point. It is robust, relatively insensitive to feature scaling, and often performs well on heterogeneous materials data without extensive tuning.

A key strength of RF is its ability to capture nonlinear relationships and feature interactions in a stable and computationally efficient way. This makes it suitable for initial comparison, particularly for the fatigue dataset, where the relationship between input descriptors and fatigue life is nonlinear but does not require explicit physical constraints. It is also less prone to overfitting than a single decision tree, as predictions are averaged over many trees trained on bootstrap samples.

RF also has some limitations. While it can capture nonlinear relationships, it does not account for metallurgical constraints, which makes it less suitable for creep prediction where the dependence on temperature and stress needs to remain physically consistent. Another issue is that its predictions are built from averaged decision trees, which can produce a less smooth response. This becomes a limitation when the model is used as a surrogate for alloy optimisation, where a stable and physically reasonable response across the design space is important.

RF was therefore used mainly as a reference model rather than a final choice. It provided a useful comparison to assess how well a simpler, robust method could describe the data. Although the results were competitive, it was less suited to the overall objectives than the selected neural-network approaches.

2.1.4. Gradient Boosted Decision Trees (GBDT)

GBDT was evaluated as a benchmark alongside the other models. Like RF, it is well suited to tabular materials datasets and can capture nonlinear relationships and feature interactions without requiring explicit feature transformation [52]. This makes it a useful option for both creep and fatigue data, particularly when descriptors vary in scale and interact in complex ways.

A key feature of GBDT is its sequential boosting strategy, where each tree is trained to correct the errors of the previous ones. This often leads to higher accuracy than bagging-based methods when the dataset contains structured but nonlinear patterns. In this case, it provided a helpful reference for assessing performance on the LCF dataset, where fatigue life depends on coupled compositional and mechanical variables. It is also well suited to datasets of moderate size, which matches the scale of the fatigue data used in this work.

However, GBDT remains entirely data-driven and does not enforce physically meaningful behaviour, which limits its use for creep prediction where consistency with temperature and stress dependence is required. The model can also be sensitive to hyperparameter choices and may overfit if not carefully controlled. While it can achieve strong interpolation within the dataset, it is less suitable when the goal is to build a physically reliable surrogate for alloy optimisation.

GBDT was therefore used as a reference for comparison. It helped assess how well nonlinear regression methods could capture the data, while also highlighting that predictive accuracy alone is not sufficient for creep modelling without physical consistency.

2.1.5. Extreme Gradient Boosting (XGBoost)

XGBoost was included as a high-performance benchmark for structured tabular data [53]. It is widely used for modelling complex nonlinear relationships and offers efficient training with built-in regularisation, making it particularly effective on datasets of limited to moderate size.

In this work, it served as a strong comparison model, especially for the LCF dataset where fatigue life depends on multiple coupled descriptors. Its ability to deliver high predictive accuracy without requiring a complex model structure made it useful for assessing whether more flexible models, such as the MLP, offered a clear advantage.

XGBoost also handles nonlinear feature interactions effectively, which is important for materials datasets where alloy composition and testing conditions are closely linked. However, like other tree-based ensemble methods, it remains purely data-driven. It does not incorporate physical constraints and is therefore less suitable for creep modelling, where monotonic trends and mechanism sensitivity need to be preserved. In addition, its predictions are not naturally aligned with a physics-informed framework, which limits its usefulness for optimisation-focused surrogate modelling.

XGBoost was therefore used as a benchmark rather than a final model. Its inclusion strengthened the overall comparison and supported the selection of PINN for creep and MLP for fatigue based on both predictive performance and consistency with the underlying physical and optimisation requirements.

2.2. Data collection and preprocessing

Two complementary predictive models, a creep model and an LCF model, were developed to enable a unified assessment of high-temperature performance in reduced-activation steels and to support subsequent multi-objective optimisation of alloy compositions. The creep and fatigue datasets used in this study were compiled from multiple literature and proprietary sources, and therefore may contain unavoidable differences in testing methodology, measurement uncertainty, and reporting format. To improve consistency, only data with clearly defined input variables, target values, and testing conditions were retained, while records with missing values, duplicated entries, or non-physical values were excluded. In addition, all data were converted into a unified descriptor space based on alloy composition, testing conditions, and derived physical or mechanical features, so that samples from different sources could be represented in a consistent numerical form. For the creep dataset, physically meaningful descriptors such as homologous temperature and diffusion-related parameters were introduced to improve comparability across different alloys and test conditions. For the fatigue dataset, mechanically derived descriptors extracted from stabilised hysteresis behaviour were used to reduce inconsistency arising from different reporting formats. All variables were then standardised before model training to improve numerical stability. Although this procedure cannot completely eliminate all inter-study variability, it provides a practical and physically meaningful framework for integrating heterogeneous published data into the present surrogate modelling study.

For the creep model, a comprehensive dataset comprising 1,199 data points was compiled from published experimental studies and proprietary sources [9,15,17,18,20,54–74] to construct a dual-mechanism PINN for predicting the creep rupture time of steels under different stress-temperature conditions. Each record included two loading variables (applied stress, σ, and testing temperature, T), fifteen alloying element concentrations (e.g., C, Cr, Ni, Mo, W, V, Ta, Nb, Al, Co, Cu, Mn, Si, S, and P), and six derived physical descriptors: atomic size mismatch ($\Delta\delta$), configurational entropy (ΔS_{mix}), valence electron concentration (VEC), effective diffusion coefficient (D_{eff}), normalised temperature ratio (T/T_{m}), and stress-to-temperature ratio (σ/T). The incorporation of elemental features is essential because alloy chemistry governs diffusion kinetics, precipitation stability, and dislocation mobility during creep [75–77]. For example, Mo and W strengthen ferritic and martensitic steels by stabilising carbide and intermetallic precipitates and delaying microstructural degradation associated with Laves phase formation [78–82]. Likewise, trace additions of V and Nb enhance lattice friction and hinder dislocation motion through combined solid-solution and precipitation strengthening, thereby improving creep resistance in Cr-Mo steels [83]. The derived physical descriptors, on the other hand, represent alloy-system interactions beyond simple composition: VEC and ΔS_{mix} describe electronic and configurational effects [84,85], $\Delta\delta$ reflects lattice distortion [86], D_{eff} captures high-temperature atomic mobility [87], and the dimensionless ratios T/T_{m} and σ/T explicitly incorporate thermodynamic and mechanical driving forces into the model [45,46]. The dataset was cleaned by removing non-physical or missing values and standardised by z-score normalisation for numerical stability. Although the above preprocessing improves consistency across the compiled data sources, a formal propagation of study-specific experimental uncertainty was not carried out in the present work, mainly because the original literature sources did not report measurement errors or uncertainty ranges in a sufficiently consistent and complete manner to allow a unified treatment across the dataset. As a result, the model error reported here should be interpreted as reflecting the combined effects of experimental scatter, inter-study variability, and model approximation error, rather than uncertainty explicitly propagated from each individual source. Table 1 provides a statistical summary of all variables in the creep dataset, including their means, standard deviations and value ranges. The alloying elements exhibit considerable variability, reflecting the diversity of steel grades and compositions reported in different studies. The thermo-physical descriptors also span broad numerical intervals, indicating the complex interplay between atomic-scale characteristics and high-temperature deformation mechanisms.

Table 1
Statistical summary of variables in the creep dataset (Composition elements in wt.%).

Variables	Mean	Standard Deviation	Maximum	Minimum
C	0.126469	0.035779	0.25	0.08
Si	0.287346	0.178398	0.86	0.03
Mn	0.488456	0.100661	0.87	0.38
P	0.011854	0.007192	0.029	0
S	0.006699	0.003981	0.022	0
Ni	0.101193	0.200474	0.9	0
Mo	0.504791	0.44853	1.22	0
Cr	5.344324	3.97293	12.9	0
W	0.950117	1.191592	3.05	0
V	0.106301	0.110865	0.3	0
Co	0.005476	0.021163	0.15	0
Ta	0.025684	0.052063	0.2	0
Nb	0.000634	0.001225	0.003	0
Cu	0.036294	0.04614	0.16	0
Al	0.006809	0.009745	0.042	0
σ (MPa)	187.2055	133.0958	619.4577	18
Temperature (°C)	580.3422	66.342	700	450
$\Delta\delta$	0.14788	0.04859	0.259131	0.059533
ΔS_{mix}	10.14375	2.836256	14.81503	5.618015
VEC	5.723831	0.268636	6.759764	5.015461
D_{eff}	1.11E-19	2.13E-19	1.02E-18	2.56E-23
T/T_m	0.367004	0.039546	0.486104	0.274983
σ/T	0.229225	0.173822	0.752545	0.018497
Time to rupture (h)	4800.242	6666.637	28827	0.1

The calculation methods of the physical features are presented in Table 2. All features and the target were standardised to enhance training efficiency and numerical stability.

To reflect the distinct deformation mechanisms operating at different temperatures, the dataset was partitioned into two regimes according to the homologous temperature T/T_{m}. The low-temperature regime ($T/T_{\mathrm{m}} < 0.4$) primarily exhibits dislocation-controlled creep, while the high-temperature regime ($T/T_{\mathrm{m}} \geq 0.4$) is dominated by diffusion and recovery mechanisms [45,46]. Separate submodels were therefore trained for each regime, allowing the network to learn regime-specific physical relationships while maintaining shared architectural and physical constraints.

The proposed dual-mechanism triple-branch PINN integrates three parallel residual subnetworks, each responsible for a distinct feature domain. The first branch encodes loading conditions (σ, T), the second processes elemental composition, and the third captures thermophysical descriptors ($\Delta\delta$, ΔS_{mix}, VEC, D_{eff}, T/T_{m}, σ/T). Each branch consists of several fully connected layers with SiLU activation, layer normalisation, and dropout regularisation, followed by a residual shortcut to preserve information flow and gradient stability. The extracted latent vectors f_1, f_2, f_3 are then fused using an attention-based fusion mechanism that adaptively balances the contribution of each domain. The attention

Table 2
Physical descriptors used in the machine learning models and their definitions.

Descriptor	Symbol	Definition	Reference
Configurational entropy	ΔS_{mix}	$\Delta S_{\mathrm{mix}} = -R\cdot\sum C_i\cdot\ln(C_i)$	[88]
Valence electron concentration	VEC	$VEC = \sum C_i\cdot VEC_i$	[84]
Effective diffusion coefficient	D_{eff}	$D_{\mathrm{eff}} = \sum C_i\cdot D_i$	[87]
Atomic size mismatch	$\Delta\delta$	$\Delta\delta = \sqrt{\sum C_i\cdot\left(1-\frac{r_i}{\bar{r}}\right)^2}$	[89]

scores are computed according to Eq. (1):

$$\alpha = \mathrm{Softmax}\left(W\left[f_1, f_2, f_3\right]\right) \tag{1}$$

where W denotes a learnable projection matrix that maps concatenated branch features into attention logits. The final fused representation is then obtained as a weighted combination of the three feature embeddings, as defined in Eq. (2):

$$f_{\mathrm{fused}} = \sum_{i=1}^{3} \alpha_i f_i \tag{2}$$

This adaptive weighting enables the network to dynamically prioritise the dominant physical factors under varying creep conditions, analogous to a scaled dot-product attention mechanism [90].

To embed metallurgical knowledge, a physics prior based on the Arrhenius-type creep law was incorporated [91], as expressed in Eq. (3):

$$y_{\mathrm{phys}} = A - n\ln\sigma + \frac{Q}{RT} \tag{3}$$

where A is a constant, n is the Norton stress exponent, Q is the activation energy for creep, $R = 8.314\ \mathrm{J\ mol^{-1}\ K^{-1}}$ is the gas constant, and T is the absolute temperature. The parameters A, n, and Q were treated as learnable within the network, permitting the model to adjust physical parameters self-consistently. A coupling coefficient k_{phys} controlled the contribution of this analytical prior to the overall output.

The total loss function combines data-driven accuracy with physics-based regularisation, ensuring that the network respects metallurgical laws while learning from experimental data. The complete formulation is given in Eq. (4):

$$L_{\mathrm{total}} = L_{\mathrm{data}} + \lambda_1 L_{\mathrm{soft}} + \lambda_2 L_{\mathrm{mono}} + \lambda_3 L_{\mathrm{bound}} + \lambda_4 L_{\mathrm{grad}} \tag{4}$$

Each λ_i is a non-negative weighting coefficient controlling the relative importance of the corresponding physics constraint.

The data-fidelity term L_{data}, shown in Eq. (5),

$$L_{\mathrm{data}} = \| y_{\mathrm{pred}} - y_{\mathrm{true}} \|_2^2 \tag{5}$$

represents the mean-squared difference between the predicted creep rupture time y_{pred} and the experimentally measured logarithmic creep rupture time y_{true}. It measures how closely the network reproduces experimental observations.

The soft-physics constraint L_{soft}, defined in Eq. (6),

$$L_{\mathrm{soft}} = \| y_{\mathrm{pred}} - y_{\mathrm{phys}} \|_2^2 \tag{6}$$

encourages the predicted lifetime to follow the analytical expression derived from the Arrhenius-type creep law.

The monotonicity constraint L_{mono}, given in Eq. (7),

$$L_{\mathrm{mono}} = \left\langle \mathrm{ReLU}\left(\frac{\partial y}{\partial T}\right) + \mathrm{ReLU}\left(\frac{\partial y}{\partial \sigma}\right) \right\rangle \tag{7}$$

penalises any unphysical increase in predicted creep rupture time with rising temperature or stress. Here $\partial y/\partial T$ and $\partial y/\partial \sigma$ denote the partial derivatives obtained through PyTorch's automatic differentiation. Because $ReLU(x) = x$ for $x > 0$ and 0 otherwise, only non-physical positive gradients contribute to this term. The angular brackets $\langle\cdot\rangle$ denote the average over the batch.

The boundary regularisation term L_{bound}, given in Eq. (8),

$$L_{\mathrm{bound}} = \langle \exp(y_i) | y_i > \bar{y} \rangle \tag{8}$$

discourages unrealistically large creep rupture time predictions. When an individual output exceeds the batch-mean value $\bar{y}$, the exponential penalty grows rapidly, pushing the prediction back toward a physically reasonable range. This prevents divergence of predicted creep rupture time at extremely low stresses or temperatures.

Finally, the gradient-smoothness term L_{grad}, given in Eq. (9),

$$L_{\mathrm{grad}} = \left\langle \left|\frac{\partial y}{\partial T}\right| + \left|\frac{\partial y}{\partial \sigma}\right| \right\rangle \tag{9}$$

limits excessive curvature of the predicted surface by penalising large gradients with respect to temperature and stress. The absolute-value operators ensure that both positive and negative slopes are treated equally, leading to a smoother and more physically continuous creep rupture time landscape.

All partial derivatives were computed by automatic differentiation within the PyTorch framework, which allows each physical constraint to be directly backpropagated during training. Consequently, the model learns not only to match the data but also to maintain thermomechanical consistency among predicted lifetime, temperature, and stress.

Following the construction of the creep model, an LCF life model was developed using a consolidated fatigue dataset compiled from literature sources [49,54,61,92–107] in which the target variable was $\log_{10}N_f$. The input features consisted of nineteen alloying elements (e.g., C, Cr, Ni, Mo, W, Ta, V, Nb, Al, Co, Cu, Mn, Si, S, and P) together with seven mechanically derived descriptors extracted from stabilised hysteresis loops: total strain amplitude ($\Delta\varepsilon_{\mathrm{total}}$), normalised stress range ($\Delta\sigma/\sigma_1$), initial flow stress (σ_1), peak stress (σ_{max}), cyclic softening rate, strain rate and testing temperature. These descriptors capture the key microstructural processes governing LCF behaviour, including dislocation rearrangement, dynamic recovery, subgrain evolution and cyclic hardening/softening behaviour. Unlike creep, LCF in the investigated temperature-strain range is governed by a single dominant deformation mechanism associated with cyclic plasticity, and does not undergo a transition in deformation mechanism that would require regime partitioning or physics constraints. Therefore, a standard multilayer perceptron was sufficient to model the nonlinear mapping from the combined compositional-mechanical feature space to $\log_{10}N_f$ with high accuracy. Table 3 presents a statistical summary of all variables the LCF dataset, including alloying elements, mechanically derived descriptors and the fatigue life target variable. For each feature, the table reports the mean, standard deviation and full value range from the minimum to the maximum, thereby quantifying the heterogeneity present across the compiled experimental studies.

After preprocessing, the dataset was randomly divided into a training set and an independent test set in a ratio of 80:20 (random seed = 42).

Table 3
Statistical summary of variables in the LCF dataset (Composition elements in wt. %).

Variables	Mean	Standard Deviation	Maximum	Minimum
Al	0.126143	0.122725	0.71	0
C	0.089258	0.034269	0.34	0.01
Co	0.115221	0.098288	0.29	0
Cr	7.020225	2.014477	9.3	1.15
Cu	0.119109	0.094855	0.29	0
Mn	0.813537	0.60713	3.2	0
Mo	0.126985	0.106851	1	0
Nb	0.119914	0.100151	0.33	0
Ni	0.767273	0.492243	1.78	0
P	0.119471	0.096788	0. 029	0
S	0.115944	0.099492	0. 029	0
Si	0.160774	0.20843	1.7	0
Ta	0.110771	0.049689	0.26	0
V	0.152723	0.086375	0.3	0
W	1.061432	0.578441	2.7	0
$\Delta\varepsilon_{total}$ (%)	0.799771	0.283065	2	0.19
σ_1 (MPa)	736.0042	170.9635	1498	240
σ_{max} (MPa)	795.3987	180.6653	1498	270
Softening rate	0.15661	0.204479	1.72	-0.41
Strain rate (s^{-1})	0.009898	0.005649	0.03	0.0001
Temperature (°C)	382.5962	146.7235	600	25
$\log_{10}N_f$	1.596233	1.914023	6	-3.58

Each sample in the compiled dataset corresponds to a single independent creep rupture test or fatigue test record with one final target value, rather than time-resolved measurements from the same experiment. Therefore, the split was performed at the data-record level, which avoids leakage of sequential measurements from the same test between training and test sets. Hyperparameter optimisation and model selection were performed using the training data only, with validation carried out during the Optuna optimisation process. The held-out test set was reserved exclusively for final evaluation. Although neural-network training is stochastic in nature, the use of fixed random seeds, together with held-out test evaluation, regularisation, and comparison with alternative models, reduces the risk that the reported conclusions depend on one favourable random initialisation alone.

Although the creep dataset contains 1,199 data points, the present model is not a large unconstrained deep neural network trained on raw high-dimensional signals, but a compact physics-informed surrogate trained on composition, testing conditions, and engineered physical descriptors. In addition, dropout regularisation, physics-based constraints, and held-out test-set evaluation were adopted to reduce the risk of overtraining. Together, these measures provide a more robust modelling framework for the present structured regression task under limited-data conditions.

To ensure consistency between the two predictive tasks, hyperparameters of both the creep PINN and fatigue MLP were optimised using Optuna Bayesian optimisation. The creep model explored network width (64-160), depth (1-4), dropout (0.1-0.5), learning rate ($1 \times 10^{-4} - 5 \times 10^{-3}$) and the physics weighting coefficients ($\lambda_1 - \lambda_4 = 10^{-5} - 10^{-2}$), whereas the LCF model explored only the architectural hyperparameters. Each search involved 20-25 trials followed by retraining of the best model for 600 epochs using the Adam optimiser. The optimal hyperparameters for each model are provided in the Supplementary Material under Hyperparameter Optimisation. The evaluation metrics for both models included *MSE*, *MAE*, *RMSE* and the coefficient of determination R^2, with their mathematical forms given in Eqs. (10-12).

$$R^2 = 1 - \frac{\sum_{i=1}^{n}(y_i - \hat{y}_i)^2}{\sum_{i=1}^{n}(y_i - \bar{y})^2} \tag{10}$$

$$RMSE = \sqrt{\frac{1}{n}\sum_{i=1}^{n}(y_i - \hat{y}_i)^2} \tag{11}$$

$$PCC = \frac{n(\sum xy) - (\sum x)(\sum y)}{\sqrt{\left[n\sum x^2 - (\sum x)^2\right]\left[n\sum y^2 - (\sum y)^2\right]}} \tag{12}$$

To verify that the selected models represented the optimal modelling choices, multiple baseline models were constructed. For creep, three additional variants were evaluated: a purely data-driven MLP without physical constraints, a single-mechanism model without temperature-based regime partitioning, and a model without either physics priors or mechanism separation. These alternatives exhibited reduced accuracy or non-physical behaviour, confirming the necessity of the dual-mechanism physics-informed architecture. For fatigue, random forest, gradient-boosted decision trees, XGBoost and MLP models were trained on the same dataset. Among them, the MLP consistently achieved the highest predictive accuracy and generalisation, validating its selection as the final LCF model.

To gain physical insight into the learned predictive behaviour, SHAP-based interpretability analysis was performed for both the creep and LCF models. Global SHAP values were used to quantify the relative influence of alloying elements and thermomechanical descriptors on model outputs, while SHAP interaction values enabled the identification of nonlinear coupling effects between key solutes (e.g., Cr-W, V-Ta, Mo-W). These analyses provided a transparent and physically meaningful interpretation of the models' decision processes and further validated their suitability for alloy design.

The two optimised surrogate models were subsequently integrated into a multi-objective optimisation framework in which alloy composition served as the design variable, and creep rupture time, together with LCF life, served as competing objectives. The optimisation was carried out using the NSGA-II evolutionary algorithm, enabling the exploration of Pareto-optimal compositions that balance long-term creep resistance with favourable cyclic deformation behaviour. The resulting Pareto front forms the basis of the alloy design strategy developed in this study.

3. Results and discussion

3.1. Model training

To comprehensively assess the predictive capability of the proposed dual-mechanism PINN, three baseline models were constructed for comparison: an MLP without physical constraints, an MLP trained without mechanism partitioning, and a simplified MLP that removes both physics priors and mechanism separation. The prediction results of these models are summarised in Fig. 2.

As illustrated in Fig. 2 (a), the dual-mechanism PINN exhibits the closest agreement with the 45° reference line, with highly concentrated scatter and minimal deviation across the full range of creep lives. The close clustering of data points confirms that the combined use of mechanism partitioning and physics-informed regularisation effectively captures the distinct deformation kinetics in different homologous-temperature regimes, resulting in high predictive fidelity and physically consistent behaviour.

The model without physics constraints in Fig. 2 (b) shows noticeably larger scatter, particularly in long-life, low-stress conditions where the sensitivity to activation energy and stress exponent becomes more pronounced. Although the overall trend is preserved, the increased dispersion indicates that purely data-driven learning struggles to maintain the correct monotonic relationship with respect to temperature and stress in the absence of physics guidance.

The model trained without mechanism partitioning in Fig. 2 (c) exhibits further deterioration in predictive accuracy. The scatter is broad, and systematic deviations from the ideal line appear across both short- and long-life regions. This result confirms that a single-mechanism formulation is unable to simultaneously represent dislocation-dominated ($T/T_m < 0.4$) and diffusion-dominated ($T/T_m \geq 0.4$) creep behaviour, leading to misrepresentation of regime-dependent deformation kinetics.

Interestingly, the simplified MLP that removes both physics priors and mechanism partitioning in Fig. 2 (d) performs slightly better than the model in Fig. 2 (c). Without being constrained by a mis-specified universal creep law, the fully data-driven MLP achieves a more balanced interpolation across the dataset, resulting in slightly reduced scatter relative to the partially constrained but incorrectly structured model. Nevertheless, its accuracy still remains significantly lower than that of the dual-mechanism PINN, highlighting the importance of both mechanism separation and physically grounded regularisation.

The collective results from the four-model comparison clearly indicate that the dual-mechanism PINN offers the best balance of accuracy, stability, and physical consistency. The robust predictive behaviour observed in Fig. 2 (a), together with the noticeable shortcomings of the single-mechanism and unconstrained models, provides strong justification for adopting the dual-mechanism physics-informed framework as the core creep rupture time predictor for the subsequent multi-objective alloy optimisation.

For fatigue, the predictive performance of several representative ML models, including MLP, RF, GBDT and XGBoost, was evaluated to identify the most suitable predictive model for LCF life. All models were trained using the same dataset, with identical preprocessing procedures and train-test splits. The corresponding prediction results are shown in Fig. 3.

As illustrated in Fig. 3 (a), the MLP model provides accurate

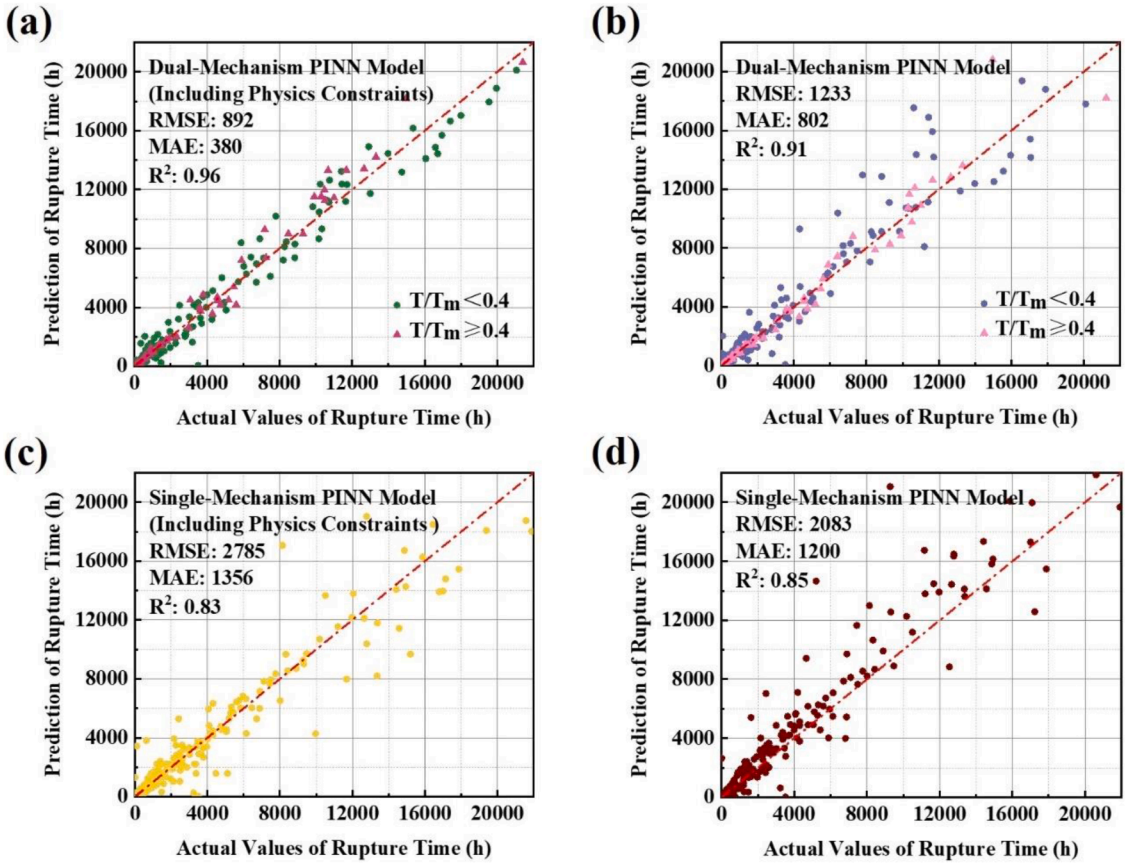

Fig. 2. Comparison of test-set creep rupture time predictions across four models: (a) dual-mechanism PINN with physics constraints, (b) dual-mechanism PINN without physics constraints, (c) single-mechanism PINN with physics constraints, and (d) single-mechanism PINN without physics constraints; the dual-mechanism physics-informed model achieves the highest overall accuracy ($R^2 = 0.96$, $MAE = 380$ h, $RMSE = 892$ h).

predictions with close alignment to the 45° reference line and a compact distribution of points across the entire life range. The model captures the nonlinear effects of strain amplitude, stress response, softening behaviour, strain rate, temperature and alloy composition, resulting in a high degree of agreement between predicted and experimental $\log_{10}N_f$ values.

A minor deviation can be observed for one sample in Fig. 3 (a), where the predicted fatigue life is lower than the corresponding experimental value. Such deviations may occasionally occur in neural-network-based models because multilayer perceptrons approximate nonlinear relationships through global function fitting. When certain samples lie in relatively sparse regions of the feature space or involve uncommon combinations of input variables, the model may produce larger prediction errors for these isolated points.

In contrast, tree-based ensemble models partition the feature space into multiple local regions through decision-tree structures, which may lead to different prediction behaviour for certain individual samples. It should also be noted that model performance is evaluated based on the overall predictive behaviour across the entire dataset rather than individual data points. Therefore, isolated deviations do not necessarily reflect the overall reliability of the model.

The RF model in Fig. 3 (b) also achieves good predictive accuracy, with the overall trend following the reference line. Compared with the MLP, the degree of scatter is slightly larger, particularly for longer fatigue lives, which suggests some limitations in representing smooth variations in cyclic deformation behaviour. Nevertheless, the model remains competitive and demonstrates the reliability of tree-based approaches for fatigue prediction.

The performance of the remaining regression models, illustrated in Figs. 3 (c, d), are likewise satisfactory. The predictions capture the overall increasing trend of $\log_{10}N_f$ and remain within a physically reasonable range, although a somewhat broader spread can be observed relative to the MLP. These results indicate that LCF behaviour in the present dataset is highly learnable across multiple modelling approaches.

Overall, all models showed strong predictive capability for fatigue life, and the differences among them were relatively modest. The MLP was selected as the final LCF model because it provided the best overall balance of predictive accuracy and generalisation on the test set. However, this does not imply that it is universally superior in every engineering context. Tree-based models such as XGBoost remained highly competitive, and may be preferable in applications where avoiding isolated large deviations is considered more important than achieving the best overall statistical performance.

3.2. Model Training Dynamics Study

The behaviour of the loss functions provides a detailed view of how the proposed modelling framework learns the underlying deformation mechanisms across both creep and LCF. Although the two deformation modes differ fundamentally in their controlling physics, the evolution and composition of the corresponding loss terms reveal how the models adapt their learning strategies to the specific characteristics of each regime.

For creep, the evolution and composition of the physics-informed loss under the dual-mechanism PINN framework clearly illustrate the model's adaptive response to distinct deformation regimes. As shown in Fig. 4 (a), corresponding to the low-temperature regime ($T/T_m < 0.4$), the total loss decreases exponentially but exhibits more pronounced fluctuations during the early optimisation stages. This behaviour reflects

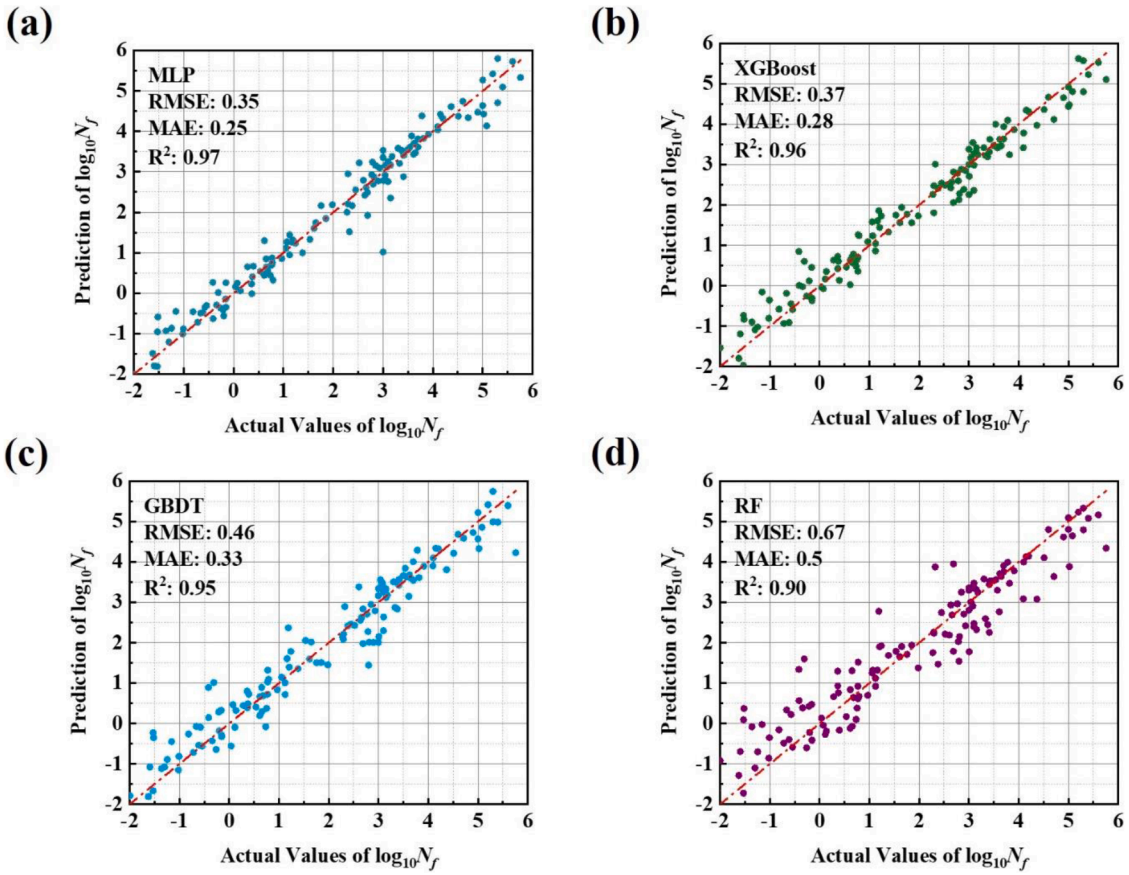

Fig. 3. Comparison of test-set LCF life predictions across four models: (a) MLP, (b) XGBoost, (c) GBDT, and (d) RF. All models show strong predictive performance, with the MLP achieving the highest accuracy ($R^2 = 0.97$, $MAE = 0.25$, $RMSE = 0.35$).

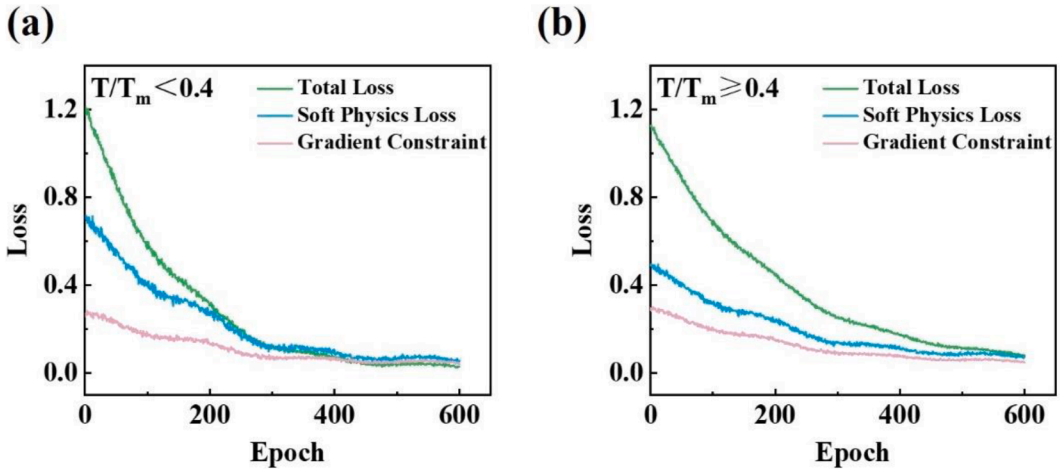

Fig. 4. Convergence behaviour of the dual-mechanism PINN showing total loss, soft physics penalty, and gradient constraint across the low-temperature (a) and high-temperature (b) creep regimes.

the complex, stress-sensitive nature of dislocation-controlled creep, where competing deformation pathways introduce stronger interactions between data fitting and physical regularisation. Consequently, the soft physics loss plays a more dominant role in stabilising the optimisation process, as evidenced by its relatively higher magnitude in this regime.

In contrast, Fig. 4 (b) shows that the high-temperature regime ($T/T_m \geq 0.4$) exhibits a smoother and more uniform convergence of both total and physics-informed loss components. This indicates that diffusion-dominated deformation mechanisms impose a more consistent physical landscape, reducing gradient competition and enabling the model to converge more steadily.

The quantitative composition of the loss provides further insight into this behaviour. As illustrated in the loss composition chart in Fig. 5, the data-driven term L_{data} contributes the largest portion of the total loss in both mechanisms, although with different magnitudes. It accounts for roughly 70.3 % of the loss in the low-temperature regime and increases to about 79.6 % at high temperature. The relative importance of the soft physics term L_{soft} decreases markedly from 18.3 % to 8.3 % as

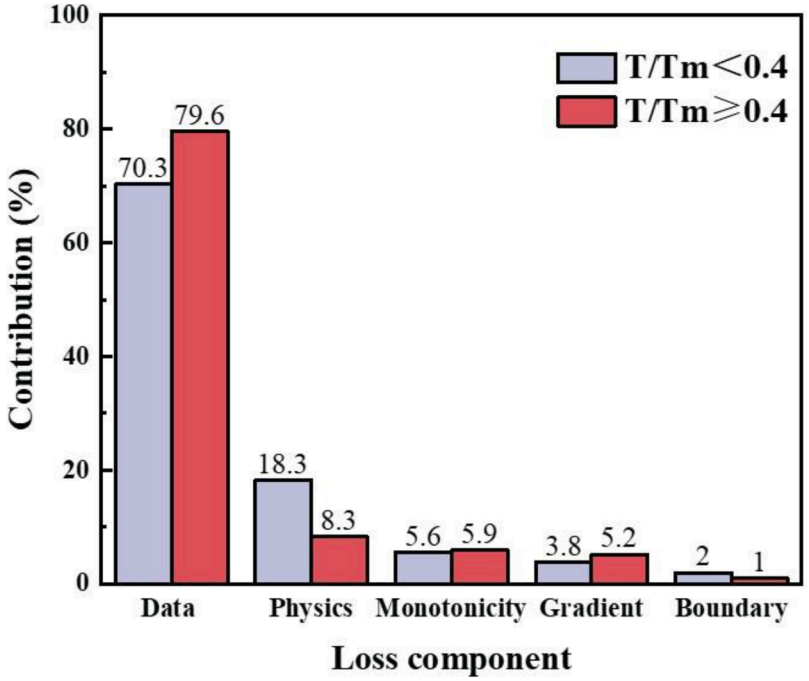

Fig. 5. Relative contribution of individual loss components in the dual-mechanism PINN for the low-temperature ($T/T_m < 0.4$) and high-temperature ($T/T_m \geq 0.4$) regimes.

temperature increases. This trend suggests that the physics constraint plays a more substantial role in the low-temperature regime ($T/T_{\mathrm{m}} < 0.4$), where creep deformation is dominated by stress-controlled dislocation mechanisms characterised by strong stress sensitivity and complex dislocation interactions. Under these conditions, incorporating physical constraints helps guide the model toward physically consistent predictions. At higher homologous temperatures ($T/T_{\mathrm{m}} \geq 0.4$), creep deformation becomes increasingly governed by thermally activated diffusion-assisted mechanisms. These processes typically follow Arrhenius-type temperature dependence and exhibit smoother kinetic behaviour compared with the strongly stress-sensitive creep observed at lower temperatures. As a result, the experimental trends become more regular, allowing the data-driven component of the model to capture the behaviour more effectively. Consequently, the model requires a smaller contribution from the physics-based constraint L_{soft}, which explains the reduced relative importance of the physics term observed in Fig. 5.

The remaining terms, including the monotonicity, gradient and boundary penalties, contribute smaller but consistent portions in both regimes, each accounting for less than 6 % of the total loss. These terms help maintain smoothness, monotonic behaviour and numerical stability without dominating the optimisation. The slightly larger gradient component at high temperature (5.2 % compared with 3.8 % at low temperature) suggests that a modest level of regularisation remains useful in conditions where diffusion becomes rapid, and stress sensitivity decreases.

Taken together, the trends observed in loss evolution and loss composition clearly reflect the underlying transition from stress-driven dislocation creep to diffusion-controlled deformation. The PINN adjusts the balance between data fidelity and physics-based penalties in a way that reflects the physics of the problem: stronger physical regularisation in the low-temperature regime ensures accurate modelling of complex, stress-dependent behaviour, while a more data-dominated regime at high temperature enables efficient learning of smoother, temperature-governed kinetics. This adaptive behaviour confirms that the proposed dual-mechanism framework maintains physical consistency across the full temperature range of creep deformation.

In contrast to creep, the learning behaviour of the LCF model exhibits a more uniform and well-conditioned loss evolution, reflecting the smoother mechanical relationships governing LCF. The training loss decreases rapidly during the initial epochs and then approaches a stable plateau, indicating efficient optimisation without significant fluctuation. This smooth convergence is consistent with the relatively regular dependence of fatigue life on strain amplitude, stress range, softening rate and strain rate, and is further illustrated by the loss curve in Fig. 6 (a), where the sharp early decline followed by a long, stable tail demonstrates that the optimisation landscape is well behaved and does not exhibit competing gradients or instability. The comparative performance curves in Fig. 6 (b) further illustrate the influence of training data size on the predictive performance of the tree-based models. As the number of training samples increases from approximately 50 to 450, the validation accuracy of all three algorithms improves steadily. For XGBoost, the validation R^2 increases from approximately 0.66 at around 50 samples to about 0.95 when the full dataset is used, indicating strong predictive capability as more training data become available. The GBDT model shows a similar trend, with R^2 rising from 0.56 to approximately 0.94 as the training dataset expands. In comparison, the RF model exhibits a slower improvement, with R^2 increasing from 0.57 to around 0.88-0.90 over the same range of training sample sizes. Overall, the continuous improvement in prediction accuracy with increasing training data indicates that the fatigue dataset contains sufficiently informative mechanical descriptors, allowing different machine-learning algorithms to effectively learn the relationship between deformation features and fatigue life.

Together, the behaviour of the loss functions across both deformation modes highlights the adaptability of the overall modelling strategy. The creep PINN dynamically balances empirical fitting and physics enforcement according to the operating mechanism, while the LCF model benefits from a smoother optimisation landscape governed by continuous cyclic deformation metrics. This combined behaviour confirms that the proposed modelling framework achieves stable, physically consistent learning across both long-term creep and cyclic fatigue, providing a robust foundation for subsequent multi-objective alloy optimisation.

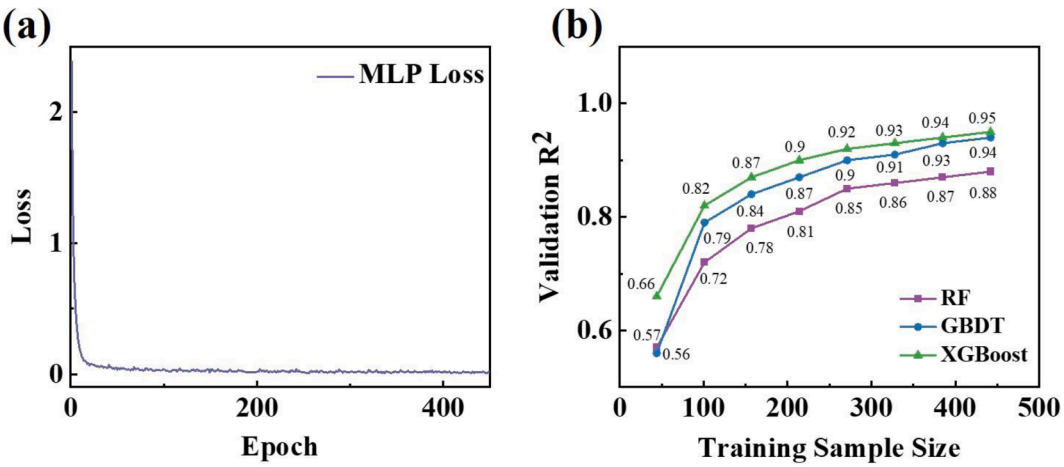

Fig. 6. Learning behaviour of the fatigue prediction model: (a) training-loss evolution of the MLP model showing smooth and stable convergence; (b) validation R^2 of different machine learning models as a function of training sample size.

3.3. SHAP Analysis for Model Interpretability

To quantitatively evaluate how each descriptor contributes to the prediction of creep rupture time and to uncover the physical pathways embedded in the dual-mechanism model, SHAP analysis was performed for both temperature regimes (Fig. 7). The results clearly delineate the shift from dislocation-dominated creep at low temperatures to diffusion-governed deformation at high temperatures, while also revealing how composition- and structure-derived descriptors influence these mechanisms.

In the low-temperature regime ($T/T_m < 0.4$), Fig. 7 (a), σ and σ/T exhibit the highest SHAP magnitudes, confirming that the creep rate is primarily governed by stress-driven dislocation motion. At such temperatures, thermal activation is insufficient to enable extensive vacancy diffusion; thus, plastic strain accumulation proceeds via dislocation glide and climb. The red-to-blue distribution of SHAP values for σ and σ/T indicates that higher applied σ or a higher σ/T strongly decreases the predicted creep rupture time, as higher dislocation density accelerates strain accumulation. This response aligns with the high stress sensitivity ($n \approx 5-7$) typical of power-law creep in ferritic and martensitic steels [108–110].

Interestingly, the microstructural parameters ΔS_{mix}, $\Delta\delta$, and *VEC* also show non-negligible contributions. A higher ΔS_{mix} corresponds to increased atomic-level chemical disorder, which increases lattice friction and suppresses dislocation mobility [111–113]. Likewise, a larger atomic-size mismatch $\Delta\delta$ introduces stronger local elastic strain fields, impeding dislocation motion and stabilising subgrains, thereby retarding creep strain accumulation. This explains why high values of ΔS_{mix} and $\Delta\delta$ produce positive SHAP effects on creep rupture time, indicating slower creep and extended time to failure [114,115]. The positive correlation between *VEC* and creep rupture time arises from its influence on the electronic structure and lattice stability of bcc alloys. An increase *VEC* enhances the d-band filling and metallic bonding strength, which stabilises the bcc lattice and reduces the lattice friction stress (Peierls stress). This facilitates dislocation glide and climb at high temperature, suppressing localised deformation and retarding creep damage accumulation, thereby extending the creep rupture time [84,116].

The elemental descriptors Cr, W, and Ta show smaller but consistently directional SHAP contributions. Cr strengthens the ferritic-martensitic lattice by stabilising fine lath and subgrain structures and promoting the formation of $M_{23}C_6$ and MX carbides along boundaries, which reduce grain-boundary diffusion and suppress the nucleation of creep cavities [117]. W provides solid-solution strengthening and promotes the formation of stable Laves and MX-type particles that effectively pin dislocations and subgrain boundaries, thereby delaying creep strain accumulation [118]. Ta further contributes by forming thermally stable TaC/TaN precipitates that inhibit dislocation climb and prevent precipitate coarsening, maintaining the integrity of the tempered microstructure during long-term exposure [119].

Taken together, the SHAP patterns in the low-temperature regime indicate that creep rupture time is controlled by the combined effects of σ, dislocation substructure evolution, and solute-induced lattice hardening. The broad SHAP scatter observed for stress-related variables reflects the complex competition between strain hardening and recovery during tertiary creep [120,121].

In the high-temperature regime ($T/T_m \geq 0.4$), Fig. 7 (b), most key descriptors exhibit negative SHAP values. This indicates that increasing these variables shortens the predicted creep rupture time. This contrasts sharply with the low-temperature regime and reflects a transition to diffusion-dominated deformation. The most influential variables, T/T_m and Temperature, both show strongly negative SHAP contributions: as temperature rises, the rate of thermally activated diffusion and dislocation climb increases exponentially, accelerating grain-boundary sliding and void growth [122–124]. Consequently, a higher T/T_m directly promotes microstructural instability and reduces creep rupture time.

D_{eff} ranks third and also displays a predominantly negative influence. This correlation highlights the central role of atomic mobility at elevated temperatures, enhanced D_{eff} facilitates vacancy migration, enabling creep strain accumulation through Nabarro-Herring and Coble diffusion pathways [88,125].

At elevated temperatures, term ΔS_{mix} ceases to act as an effective diffusion barrier because thermal activation overwhelms the local lattice distortions; in fact, increased disorder may facilitate atomic exchange and defect generation, thereby accelerating diffusion-controlled creep [126]. Similarly, a higher *VEC* may reduce the activation energy for diffusion by weakening directional bonding in bcc solid solutions [84]. Likewise, $\Delta\delta$ induced lattice distortion, while beneficial at moderate temperatures, may lose its diffusion-retarding effect at high homologous temperatures, enabling enhanced atomic mobility [127,128].

Cr and W exhibit weakly negative SHAP effects, consistent with their tendency to promote microstructural degradation at elevated temperatures. Cr-rich $M_{23}C_6$ carbides readily coarsen during prolonged creep, causing Cr depletion along boundaries and reducing interfacial pinning, which facilitates grain-boundary sliding and void growth [129,130]. W contributes to solid-solution and precipitation strengthening at intermediate temperatures, but at higher temperatures, it segregates into coarse Laves phases, diminishing its strengthening effect [118]. In contrast, Ta displays a positive SHAP influence owing to the superior thermal stability of TaC/TaN precipitates, which effectively suppress

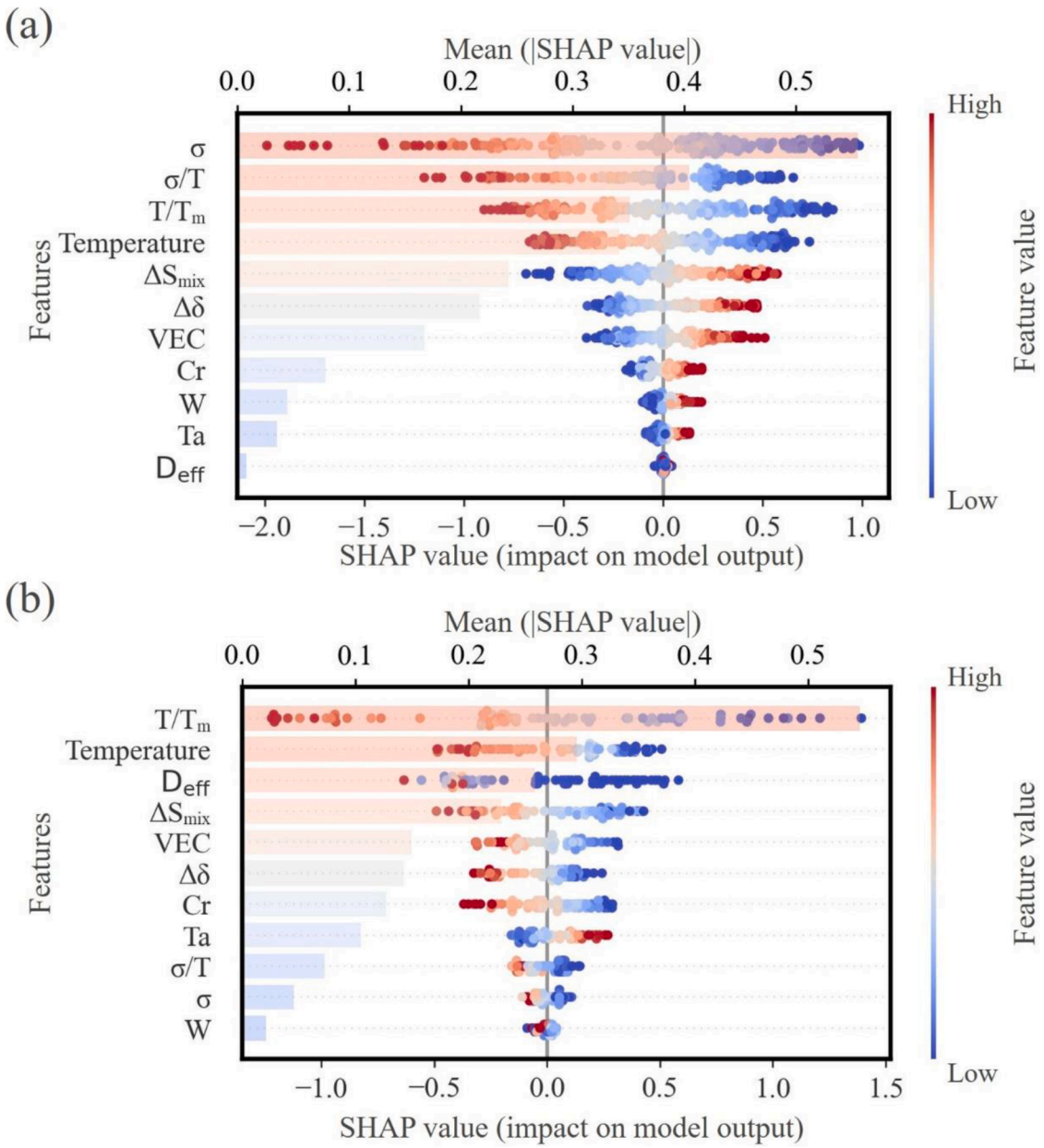

Fig. 7. SHAP summary plots showing feature importance and directional influence for the dual-mechanism PINN under (a) low-temperature ($T/T_m < 0.4$) and (b) high-temperature ($T/T_m \geq 0.4$) creep regimes.

dislocation climb and subgrain coalescence, thereby preserving creep strength [131,132].

Collectively, these SHAP patterns confirm that the high-temperature mechanism is governed by temperature-controlled diffusion and recovery, rather than stress-induced dislocation processes. The near-universal negative SHAP values emphasise that all thermal and compositional parameters, except for refractory elements such as Ta, ultimately contribute to microstructural degradation when thermally activated processes dominate. This model interpretation is consistent with classical high-temperature creep theory and experimental observations in ferritic and martensitic steels operating above 0.4 T_m.

For further validation, the mechanisms revealed by the SHAP analysis can be compared with the behaviour reported for other structural materials used in nuclear reactors, such as martensitic HT-9 steel and austenitic stainless steels including 316FR and 316LN. Ferritic-martensitic steels such as HT-9 are widely used in fast reactors because of their good swelling resistance and thermal conductivity. Their creep behaviour is typically controlled by stress-assisted dislocation motion at lower homologous temperatures, while diffusion-controlled mechanisms dominate at higher temperatures [133]. This transition is consistent with the mechanism shift identified in the present SHAP analysis.

Austenitic stainless steels such as 316FR and 316LN are commonly used for reactor internal structures due to their good creep ductility and resistance to creep-fatigue damage. Their creep rupture strength is strongly influenced by microstructural stability and precipitation behaviour during long-term exposure at 550-600°C [134]. Similar studies have also shown that creep deformation and rupture behaviour in steels such as 316LN and HT-9 can be described using damage-based models involving cavity growth and microstructural degradation [135]. These observations agree well with the present SHAP results, where temperature-dependent diffusion and microstructural descriptors play a dominant role at higher homologous temperatures [136].

Overall, the agreement between the SHAP-derived mechanisms and

the experimentally observed behaviour of established reactor steels further supports the physical reliability of the present model.

For fatigue, the SHAP patterns highlight a distinctly different hierarchy of controlling variables, reflecting the transition from time-dependent creep mechanisms to strain-controlled cyclic deformation (Fig. 8). The resulting beeswarm map reveals a highly ordered hierarchy of controlling variables and clearly separates strain-controlled fatigue behaviour from thermally activated deformation and alloy-chemistry effects. The SHAP distribution also reveals how microstructural stability, solute strengthening and time-dependent deformation jointly regulate crack initiation and propagation in ferritic-martensitic steels.

In line with classical LCF mechanics, the total strain range $\Delta\varepsilon_{total}$ exhibits the largest SHAP magnitude, confirming its dominant role in determining fatigue life. High $\Delta\varepsilon_{total}$ values (red points) strongly reduce life, whereas low-amplitude cycles (blue) shift the SHAP response into the positive region. This behaviour mirrors the Coffin-Manson relation, where plastic strain amplitude directly controls the accumulation of cyclic damage via slip localisation, dislocation band formation, and the early nucleation of microcracks on persistent slip bands [137–139].

Temperature ranks second in SHAP importance and shows a similarly smooth red-to-blue gradient. Elevated temperatures lead to strongly negative SHAP values, indicating accelerated fatigue life reduction. This reflects the thermally promoted recovery of dislocation networks, coarsening of $M_{23}C_6$ and MX precipitates, and subgrain growth, all of which destabilise the tempered martensite lath structure and promote cyclic softening [49,140,141].

The transition metals W, Ta and Cr display the next set of influential SHAP responses and collectively encode the alloy-chemistry contribution to fatigue resistance. W shows a predominantly positive SHAP pattern, especially at moderate-high W contents, indicating its stabilising role in cyclic deformation. W is well-known to strengthen ferritic-martensitic steels through a combination of solid-solution strengthening and the promotion of W-rich carbides and Laves precursors, both of which inhibit dislocation rearrangement and suppress softening under cyclic loads [99,142].

Ta also yields positive SHAP contributions across most of the composition space. This behaviour corresponds to the formation of thermally stable TaC/TaN MX precipitates, which strongly pin lath boundaries and retard recovery, thus delaying crack nucleation and enhancing resistance to cyclic strain accumulation [143].

Cr, although ranked slightly lower, exhibits a consistent positive SHAP trend; Cr stabilises the tempered martensite lath structure, promotes $M_{23}C_6$ precipitation at boundaries, and improves oxidation resistance under high-temperature cycling, all of which are known to mitigate microcrack coalescence in FM steels [144–146].

Microstructural descriptors associated with deformation stability, namely softening rate and strain rate, also show substantial contributions. A high softening rate drives SHAP values strongly negative, reflecting rapid loss of back-stress hardening, dislocation recovery, and coarsening of boundary carbides. Conversely, lower softening responses produce positive SHAP shifts, consistent with microstructures that retain lath integrity and resist cyclic rearrangements [147]. The Strain rate descriptor reveals that slow cycling reduces life (negative SHAP), whereas higher strain rates tend to suppress diffusion-assisted recovery and environmental interactions, producing more positive SHAP responses [141]. This agrees with the mechanistic understanding that slower cycling allows time-dependent processes such as creep-assisted slip, oxidation-assisted crack growth, and subgrain coarsening to participate in the fatigue response [148].

Lower-ranked solutes such as Si and Mn exhibit only modest SHAP magnitudes, which is expected because their contents are tightly controlled in RAFM steels. These elements vary within very narrow specification limits to maintain stable deoxidation behaviour, appropriate hardenability and the integrity of the tempered-martensite microstructure. As a result, the limited compositional range of Si and Mn prevents them from producing strong statistical signals in the SHAP decomposition.

Similarly, elements such as Mo, Ni, Nb, Co, Cu, and Al contribute only weakly to the SHAP response. In RAFM alloy design, these solutes are strictly restricted for reasons related to nuclear activation, phase stability and microstructural reliability [149,150]. Their allowable ranges are therefore extremely narrow, and the small compositional variation naturally leads to minimal SHAP contributions. Although these elements play important metallurgical roles in carbide stability, grain-boundary chemistry and precipitation behaviour, the constrained compositional window limits their influence on the model's feature attribution.

Collectively, the SHAP distributions portray a physically coherent fatigue landscape governed by the interplay of imposed cyclic plasticity ($\Delta\varepsilon_{total}$), thermally activated recovery (Temperature), microstructural stability (Softening rate, Strain rate), and precipitation-strengthened alloy chemistry (Cr-W-Ta). The broad SHAP scattering observed for

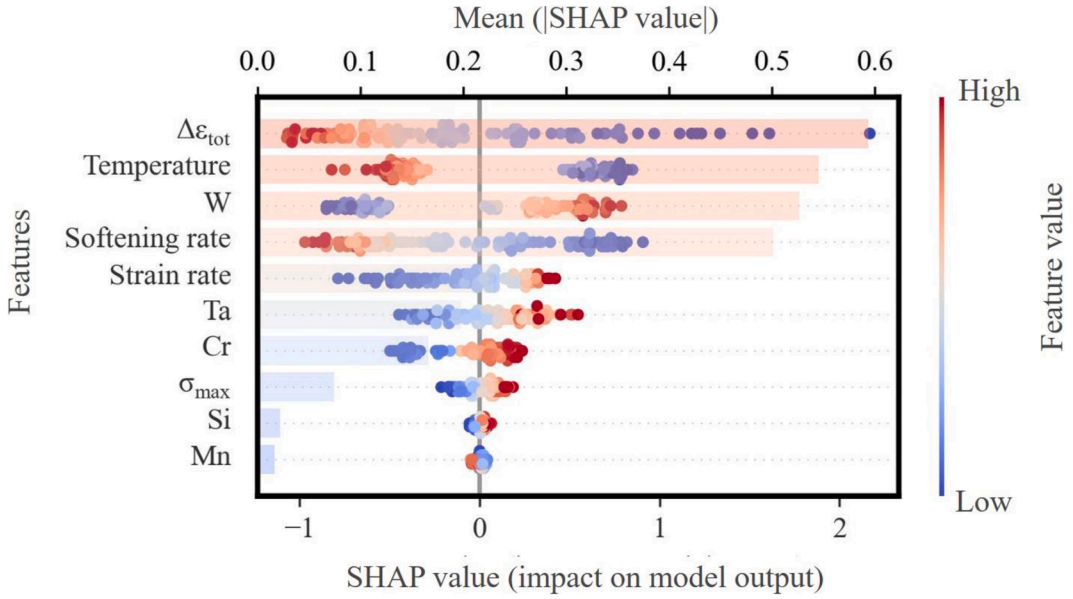

Fig. 8. SHAP summary plot showing feature importance and directional influence for the LCF prediction model.

$\Delta\varepsilon_{total}$ and Temperature reflects the inherent variability of cyclic softening, competing hardening-recovery processes, and microcrack evolution in FM steels under LCF conditions, consistent with observations in 9-12Cr and RAFM systems.

These SHAP-derived fatigue mechanisms are also consistent with experimental observations reported for structural materials used in nuclear reactor systems. For example, LCF experiments on the ferritic-martensitic steel HT-9 demonstrate that cyclic deformation behaviour is strongly temperature dependent. When the testing temperature increases from room temperature to about 600°C, HT-9 exhibits pronounced cyclic softening associated with dislocation rearrangement, subgrain formation, and precipitate redistribution along subgrain boundaries [151]. Microstructural observations further show that the tempered martensite lath structure progressively evolves into a polygonised or equiaxed subgrain structure at elevated temperatures, while carbides redistribute along the subgrain boundaries, leading to a reduction in internal stress and fatigue resistance [152]. These temperature-dependent microstructural changes closely correspond to the SHAP trends identified in the present work, where temperature and softening-related descriptors strongly influence fatigue life.

Similar fatigue mechanisms have also been reported in austenitic steels widely used in nuclear reactor components, such as 316FR, 316LN, and 316L stainless steels. Under strain-controlled low-cycle fatigue conditions, these alloys typically exhibit an initial cyclic hardening stage followed by gradual cyclic softening due to dislocation multiplication, rearrangement of dislocation structures, and microcrack initiation during cyclic plastic deformation [153]. In addition, thermomechanical fatigue studies on austenitic stainless steels show that fatigue life is strongly governed by strain amplitude, temperature, and microstructural damage mechanisms including dislocation cell formation, oxidation-assisted cracking, and dynamic strain aging effects [154]. The dominant SHAP influence of total strain range and temperature observed in the present model therefore agrees well with these experimentally observed fatigue mechanisms.

Overall, the consistency between the SHAP-derived feature hierarchy and the experimentally observed fatigue behaviour of representative reactor structural steels further supports the physical reliability and interpretability of the present fatigue prediction model.

3.4. Element Interaction Analysis

Building on the insights obtained from the SHAP beeswarm analysis in the previous section, it becomes clear that Cr, W and Ta consistently emerge as influential elements in both creep and LCF regimes. Although their individual effects are evident from the feature-attribution trends, the deformation behaviour of ferritic and martensitic steels is often governed not only by the contribution of individual alloying elements but also by the cooperative or competing interactions among them. This is particularly relevant for Cr, W and Ta, which participate simultaneously in solid-solution strengthening, carbide and Laves phase precipitation, and high-temperature diffusion processes. Their combined influence can therefore deviate substantially from the linear superposition of individual effects.

Given this metallurgical context, examining the pairwise interactions among Cr, W and Ta is essential for understanding how these elements jointly affect deformation resistance across different temperature regimes. SHAP interaction scatter plots provide a useful means to visualise how the marginal effect of one element varies as the concentration of a second element changes, thereby revealing potential synergistic or antagonistic relationships that cannot be captured by single-feature attributions alone. As shown in Fig. 9 (a-c), Cr, W, and Ta are the three most influential elemental descriptors governing creep rupture time in the low-temperature regime ($T/T_m < 0.4$). The SHAP interaction plots reveal pronounced positive cooperative effects among these elements, where simultaneous enrichment enhances creep rupture time, while their imbalance or depletion reduces it.

In the Cr-W map, a strong positive correlation at high Cr and W contents indicates a synergistic effect arising from the complementary roles of these solutes in strengthening the ferritic-martensitic matrix. Previous studies on Fe-Cr-W alloys and RAFM steels have shown that the simultaneous addition of Cr and W significantly enhances high-temperature strength and creep resistance by stabilising the martensitic microstructure and suppressing diffusion-controlled deformation mechanisms [57,76]. For example, W is widely recognised as one of the most effective solid-solution strengthening elements in ferritic steels and can substantially increase creep rupture strength at elevated temperatures [155,156], while Cr contributes to the stability of the tempered martensitic structure and improves oxidation resistance in high-temperature environments [157]. In particular, Cr stabilises the tempered martensitic lath structure and promotes the formation of

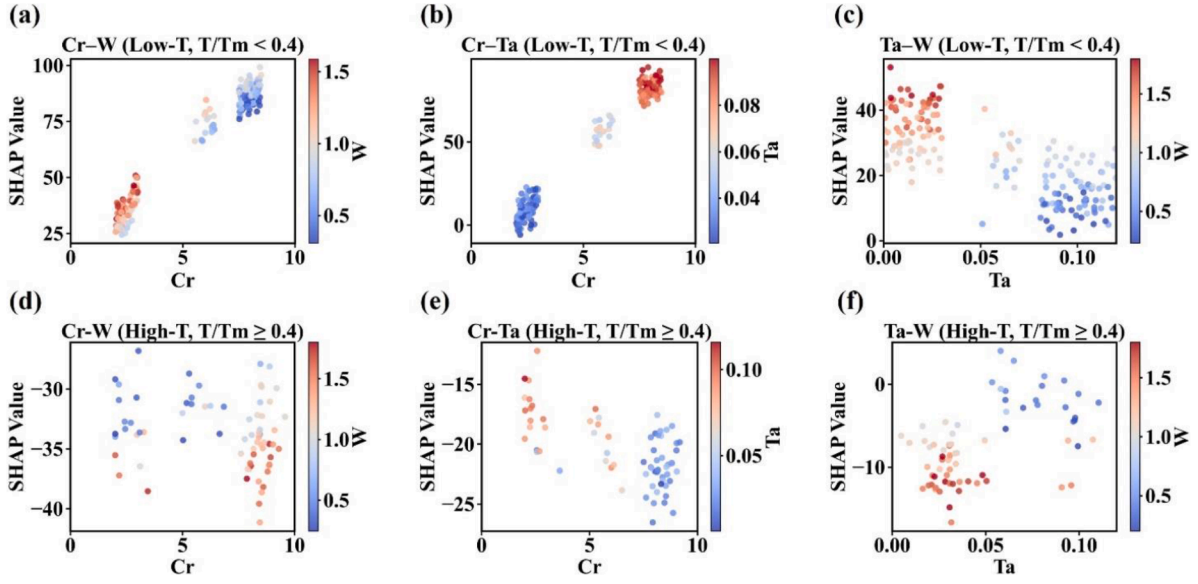

Fig. 9. Pairwise SHAP interaction plots for Cr-W, Cr-Ta and Ta-W under (a-c) low-temperature ($T/T_m < 0.4$) and (d-f) high-temperature ($T/T_m \geq 0.4$) creep regimes, illustrating how solute interactions vary across mechanisms and thermal conditions.

intergranular $M_{23}C_6$ carbides, which impede grain-boundary sliding and recovery [14,158]. These carbides preferentially form along prior-austenite and lath boundaries, acting as effective barriers to boundary migration and diffusion processes, which are critical mechanisms controlling creep deformation in ferritic-martensitic steels [158]. W, on the other hand, provides both solid-solution hardening and promotes fine Laves/MX precipitation, which efficiently pins dislocations and retards subgrain coarsening [159,160]. The presence of W has also been reported to delay microstructural degradation and enhance the stability of the lath martensite structure during long-term exposure at high temperature [118,155], thereby improving creep strength in Fe-Cr-based alloys. Therefore, the combined enrichment of Cr and W contributes to both precipitation strengthening and solid-solution strengthening, which suppresses grain-boundary diffusion, dislocation climb and subgrain coarsening. This synergistic strengthening mechanism is consistent with the strong positive SHAP responses observed in the present analysis.

The Cr-Ta relationship exhibits a similarly cooperative pattern. Ta substitutes for high-activation Nb and forms nanoscale TaC /TaN particles that possess higher dissolution temperatures and slower coarsening kinetics than $M_{23}C_6$, providing long-term pinning stability [132,159]. Elevated Ta content amplifies the beneficial effects of Cr by compensating for $M_{23}C_6$ coarsening through additional MX-type pinning, thereby maintaining the integrity of the lath/subgrain network [2,161].

In contrast, the Ta-W plot shows a more complex interaction, implying partial competition between these solutes. While both W and Ta contribute to MX-type precipitation, excessive W addition can promote coarse Laves phase formation, consuming W from solid solution and potentially hindering TaC stability [160,162]. Hence, a moderate W-Ta ratio yields the highest SHAP response, suggesting that their relative balance is critical for sustaining microstructural stability and delaying creep strain accumulation.

Overall, these inter-element SHAP interactions reveal that under low-temperature creep, Cr, W and Ta cooperate to stabilise the tempered martensitic microstructure via complementary mechanisms, including Cr-driven boundary pinning, W-assisted solid-solution hardening and Ta-based MX stability, thereby collectively enhancing creep rupture time.

With increasing temperature, the deformation mechanism of the steels gradually transitions from dislocation-controlled to diffusion-controlled creep, and the strengthening contributions of substitutional solutes become progressively less effective. As shown in Fig. 9 (d-f), the SHAP interaction plots for Cr, W, and Ta in the high-temperature regime ($T/T_m \geq 0.4$) display uniformly negative trends, indicating that their enrichment no longer enhances but rather deteriorates the creep resistance. This degradation behaviour reflects the onset of thermally activated diffusion, solute segregation, and precipitate coarsening, which collectively outweigh the beneficial effects of solid-solution and precipitation hardening at lower temperatures.

In the Cr-W map, the pronounced negative SHAP responses at high Cr and W concentrations indicate a strong synergistic degradation mechanism. In RAFM steels, $M_{23}C_6$ carbides are recognised to coarsen significantly during long-term exposure, thereby degrading microstructural stability [131]. Although a direct study of Cr-enrichment in RAFM steels remains sparse, the mechanism observed in high-Cr creep-resistant steels suggests that Cr promotes $M_{23}C_6$ formation and grain-boundary coarsening [163]. Simultaneously, W accelerates the precipitation of Fe_2W-type Laves phases at subgrain boundaries, consuming W from solid solution and thereby weakening solid-solution strengthening [164,165]. The concurrent coarsening of $M_{23}C_6$ and Laves phases promotes grain-boundary sliding and void growth, explaining the strongly negative SHAP contributions in the Cr-W domain.

The Cr-Ta interaction map exhibits a similar trend but with less severity, suggesting that Ta partially mitigates the detrimental influence of Cr at high temperatures. While Cr-induced $M_{23}C_6$ carbides remain coarsening-prone, Ta promotes the formation of thermally stable TaC and TaN precipitates that resist Ostwald ripening and maintain pinning efficiency under long-term exposure [166,167]. While MX-type precipitates are relatively stable against coarsening, sustained high-temperature exposure still promotes their gradual coarsening and interface relaxation, diminishing their subgrain boundary pinning effect. Consequently, the Cr-Ta relationship remains largely negative but with local fluctuations that suggest limited retention of strengthening through MX-phase stability.

The Ta-W interaction plot shows an overall weakly negative relationship, reflecting a competition between Ta-based MX precipitation and W-driven Laves-phase formation. At high W and low Ta levels, the diffusion of W towards subgrain boundaries promotes the growth of Laves aggregates, accelerating matrix softening [168,169]. Conversely, at moderate Ta contents, the presence of stable TaC precipitates locally retards Laves formation by tying up carbon and nitrogen, delaying phase coarsening and preserving dislocation pinning [166]. This interplay results in a diffuse scatter of SHAP values rather than a monotonic dependence, consistent with competing diffusion and precipitation kinetics.

Overall, these high-temperature SHAP interaction maps highlight a collective degradation mechanism wherein Cr, W, and Ta lose their cooperative strengthening behaviour observed at lower temperatures. The dominance of diffusion-assisted coarsening of $M_{23}C_6$ and Laves phases, combined with the partial destabilisation of MX precipitates, results in microstructural instability and reduced creep rupture time. This interpretation aligns with previous creep studies on RAFM steels, where the long-term strength degradation at high homologous temperatures is governed by solute redistribution and precipitate coarsening rather than dislocation hardening.

For fatigue, Fig. 10 presents the pairwise SHAP interaction maps for the key solute elements, illustrating how W, Cr and Ta jointly influence the model response through their coupled effects. Similar to the creep analysis, the LCF model also reveals the synergistic interactions among Cr, W and Ta, capturing how their interactions shape the predicted fatigue performance beyond their individual contributions.

The W vs Cr interaction map highlights a more pronounced cooperative effect between W and Cr, as shown in Fig. 10 (a), with both solutes producing positive SHAP contributions when present at moderate to high levels. This pattern reflects the complementary strengthening roles of W and Cr: Cr stabilises lath and boundary carbides and reduces oxidation-assisted crack advance, while W provides strong solid-solution strengthening and promotes precipitates that impede dislocation glide and climb during cyclic strain accumulation [170,171]. The upper cluster of high-Cr and high-W compositions shows consistently positive SHAP values, indicating improved resistance to fatigue-induced substructure degradation.

The SHAP interaction plot of Cr vs Ta shows that the dominant gradient arises from Cr rather than Ta, as shown in Fig. 10 (b). Increasing Cr content produces progressively more positive SHAP values, reflecting the well-established role of Cr in stabilising the tempered-martensite lath structure and suppressing microstructural degradation during cyclic loading. Cr promotes the precipitation of $M_{23}C_6$ carbides along lath and prior-austenite boundaries, enhances boundary cohesion, reduces oxidation-assisted crack advance, and maintains subgrain stability, all of which increase the number of cycles required for crack initiation [172]. These mechanisms are consistent with the monotonic positive trend seen across the 2-10 wt.% Cr range, irrespective of Ta content. The colour distribution shows no systematic dependence on Ta, indicating that small Ta variations in this dataset do not measurably perturb Cr-controlled strengthening.

The W vs Ta map similarly indicates that W is the principal driver of the observed SHAP separation, Fig. 10 (c). The SHAP values become increasingly positive when W exceeds roughly 1 wt.%, which agrees with the known role of W in enhancing cyclic stability through solid-solution strengthening and the formation of W-rich carbides and

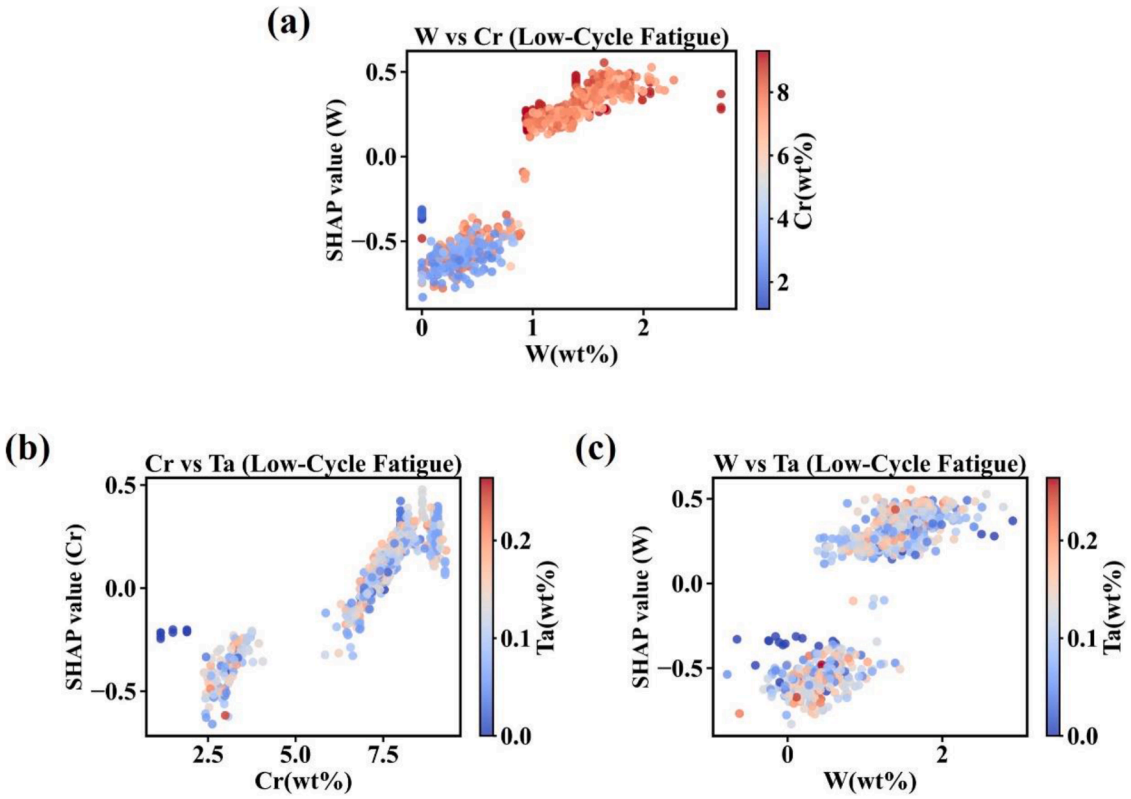

Fig. 10. Pairwise SHAP interaction plots for key solutes under LCF conditions: (a) W-Cr, (b) Cr-Ta, and (c) W-Ta. Illustrate how coupled solute effects shape the model response.

Laves-precursor clusters. These second-phase particles inhibit dislocation rearrangement, retard subgrain recovery and delay the onset of cyclic softening, thereby extending the fatigue life [20,99]. The Ta colour bar again shows no discernible clustering or directional gradient: points at different Ta levels occupy overlapping SHAP bands, demonstrating that Ta does not significantly modulate the W-controlled fatigue response within the narrow Ta window of this dataset.

The absence of any clear Ta-related synergy across the three fatigue maps can be rationalised by mechanistic considerations. Ta contributes to fatigue resistance mainly via the formation of thermally stable TaC /TaN MX precipitates, a mechanism highly effective in creep or long-term high-temperature exposure but much less influential under LCF, where cyclic softening is dominated by dislocation rearrangement rather than precipitate coarsening [142,143].

Consequently, the SHAP response under fatigue is governed almost entirely by Cr and W, with Ta showing neither a directional effect nor measurable interaction within the explored composition space.

3.5. Concurrent Optimisation of Creep and LCF Performance Using NSGA-II

Building on the high predictive accuracy demonstrated by both surrogate models in the previous sections, together with their physically consistent SHAP interpretations, a multi-objective alloy optimisation framework was developed to identify compositions that simultaneously enhance creep resistance and LCF life. The two surrogate models, namely the dual mechanism physics-informed creep PINN and the MLP-based LCF predictor, provide reliable and mechanistically interpretable performance estimators, which makes them suitable for high-dimensional optimisation tasks.

The design variable in the optimisation is the alloy composition vector, defined in Eq. (13). Iron is treated as the balance element such that the total mass fraction of solutes remains below 100 percent.

$$x = [C,\ Si,\ Mn,\ P,\ S,\ Cr,\ W,\ Ta,\ V,\ldots] \tag{13}$$

The first objective function corresponds to creep performance. A normalised squared improvement metric was selected because it enhances optimisation stability and amplifies meaningful deviations from the Eurofer97 baseline. The formulation is given in Eq. (14), where $t_r(x)$ denotes the predicted rupture time and t_r^{Euro} is the experimentally reported rupture time of Eurofer97 under identical loading conditions.

$$f_1(x) = -\left(\frac{t_r(x) - t_r^{Euro}}{t_r^{Euro}}\right)^2 \tag{14}$$

The second objective function represents fatigue life. Because fatigue mechanisms scale naturally with logarithmic life, the function in Eq. (15) was adopted.

$$f_2(x) = -\left(\frac{\log_{10}N_f(x) - \log_{10}N_f^{Euro}}{\log_{10}N_f^{Euro}}\right)^2 \tag{15}$$

Together, these definitions specify the bi-objective minimisation problem shown in Eq. (16).

$$\min_x F(x) = [f_1(x),\ f_2(x)] \tag{16}$$

To ensure practical relevance, a feasibility constraint was implemented as shown in Eq. (17). Each candidate alloy must equal or exceed the performance of Eurofer97 in both creep and fatigue.

$$t_r(x) \geq t_r^{Euro},\ \log_{10}N_f(x) \geq \log_{10}N_f^{Euro} \tag{17}$$

All fixed experimental parameters used as surrogate model inputs were taken directly from published Eurofer97 datasets. These values are summarised in Table 4. For the LCF model, the imposed conditions were 550°C, a total strain range of 0.8 %, a strain rate of 3×10^{-3} s^{-1}, an initial stress of 440 MPa, a peak stress of 450 MPa, a stress ratio of 0.32

Table 4
Summary of design variables, fixed testing conditions, model inputs and NSGA-II parameters used for multi-objective alloy optimisation.

Category	Item	Specification
Optimisation Variables	Design variables	15 alloying elements: C, Si, Mn, P, S, Ni, Mo, Cr, W, V, Co, Ta, Nb, Cu, Al
	Composition constraint	Solute elements sum $\leq$ 100 wt.% (Fe as balance)
LCF model Conditions	Temperature	550 °C
	Total strain range $\Delta\varepsilon_{total}$	0.8 %
	Strain rate	3×10^{-3} s^{-1}
	Initial stress $\sigma_{,}$	440 MPa
	Peak stress σ_{max}	450 MPa
	Stress ratio $\Delta\sigma/\sigma_1$	0.32
	Softening rate	−0.15
	Model output	$\log_{10}N_f$
Creep Model Conditions	Temperature	650 °C
	Applied stress	75 MPa
	Mechanism selection	Automatic based on T/T_m, using the dual-mechanism PINN
	Physics descriptors	$\Delta\delta$, ΔS_{mix}, *VEC*, D_{eff}, T/T_m and σ/T computed from composition and testing conditions
	Model output	Rupture time (h)
NSGA-II Configuration	Population size	200
	Number of generations	300
	Objective 1	Maximise predicted creep rupture time by minimising negative rupture time
	Objective 2	Maximise predicted fatigue life by minimising negative $\log_{10}N_f$
	Crossover operator	Simulated binary crossover with probability 0.90 and distribution index 20
	Mutation operator	Polynomial mutation with probability 1 divided by 15 and distribution index 25
	Selection strategy	Binary tournament with nondominated sorting and crowding distance
	Feasibility constraint	Solutions must exceed Eurofer97 baseline creep and fatigue performance
Surrogate Model Structure	Creep PINN input	15 elements, stress, temperature and six physics descriptors
	Fatigue MLP input	15 elements and fixed LCF test parameters
	Outputs to optimiser	Creep rupture time and fatigue life

and a softening rate of −0.15. For the creep model, the rupture tests were evaluated at 650°C and an applied stress of 75 MPa. For every candidate composition, the physics descriptors required by the dual mechanism PINN, namely $\Delta\delta$, ΔS_{mix}, *VEC*, D_{eff}, T/T_m and σ/T, were calculated analytically using the design vector and the fixed loading conditions given in Table 4. It should be emphasised that the 650°C condition adopted in this study does not represent the current operating limit of conventional RAFM steels. Rather, it serves as a forward-looking evaluation condition to assess the potential of the proposed framework for designing next-generation RAFM steels with improved creep resistance under more demanding service conditions relevant to future advanced reactor systems. The optimisation was carried out using the NSGA II evolutionary algorithm. Its configuration details, including population size, number of generations, crossover and mutation operators, and selection strategy, are listed in Table 4. NSGA II was selected because it provides excellent preservation of nondominated diversity, allows clear identification of Pareto fronts in nonconvex design spaces, and can capture strong competition between creep resistance and fatigue performance. At each generation, two hundred candidate alloys were evaluated by the surrogate models. Nondominated sorting and crowding distance ranking were then applied to construct the next population over three hundred generations. Consistent with established reduced activation ferritic-martensitic design guidelines, alloys containing Ni, Co, Cu, Nb and Al were excluded from the search space [149,150].

Under these settings, the optimisation converged to a well-defined Pareto front that characterises the achievable balance between creep rupture time and cyclic softening resistance. Four representative Pareto optimal alloys obtained from this framework are listed in Table 5. These compositions illustrate the natural trade offs between C, Si, Mn, Cr, W, Ta and V when creep and fatigue performance are enhanced simultaneously. The predicted fatigue lives $\log_{10}N_f$ of 3.85 to 4.18 exceed those of Eurofer97 under identical loading conditions. The predicted creep rupture lives at 650°C and 75 MPa fall within the range of 2500 to 5090 hours, also surpassing the performance of Eurofer97.

The predicted creep rupture time obtained in this study should be interpreted within the design constraints of RAFM steels intended for fusion reactor structural components. Unlike conventional high-temperature steels, the composition space of RAFM steels is strictly restricted by low-activation requirements, which limit the use of several alloying elements commonly employed to enhance creep strength. For example, elements such as Nb, Ni, Mo, and Cu must be maintained at very low levels or avoided to minimise long-term radioactive activation under neutron irradiation [149,150]. Furthermore, the creep resistance of oxide dispersion strengthened (ODS) steels is primarily achieved through a fundamentally different strengthening mechanism involving a high density of stable nanoscale oxide particles introduced via mechanical alloying and powder-metallurgy processing routes [173,174]. Such specialised processing strategies are not considered in the present work, which focuses on composition design within the framework of conventionally produced RAFM steels. Therefore, the predicted creep performance should be evaluated relative to existing RAFM reference alloys, such as Eurofer97, rather than directly compared with ODS steels or unconstrained high-temperature alloy systems.

A closer inspection of the optimised compositions reveals several metallurgically reasonable trends. The relatively high Cr content maintains the ferritic-martensitic matrix stability and contributes to oxidation resistance at elevated temperatures [175]. W and Ta act as strong precipitation-strengthening elements and play an important role in improving creep resistance through the formation and stabilisation of fine carbides or intermetallic particles [20,99]. Meanwhile, moderate additions of C, Mn and Si help stabilise the martensitic microstructure and influence cyclic deformation behaviour [176,177].

The optimisation process therefore converges toward compositions that balance precipitation strengthening, solid-solution strengthening and microstructural stability, which are all known to be critical factors governing creep rupture and fatigue performance in RAFM steels. This agreement with established metallurgical principles further supports the reliability of the optimisation results. These findings confirm that the combined PINN-MLP-NSGA II framework can identify compositions with balanced and simultaneously improved performance across both deformation regimes.

4. Conclusion

In this study, physics-informed and data-driven surrogate models were integrated with multi-objective optimisation to enable concurrent design of creep- and fatigue-resistant reduced-activation steels. The key findings are summarised as follows:

1. **Creep modelling** - The dual-mechanism PINN achieves $R^2 = 0.96$, and its loss decomposition shows that although both temperature regimes remain predominantly data-driven, the influence of physical constraints is substantially stronger at low temperature ($T/T_m < 0.4$, $L_{soft} = 18.3\%$) than at high temperature (8.3%), demonstrating adaptive learning fully consistent with the temperature-dependent evolution of creep kinetics.

Table 5
Alloy compositions generated by the NSGA-based multi-objective optimisation and their predicted fatigue and creep rupture time.

Alloy	C	Si	Mn	Cr	W	Ta	V	$\log_{10}N_f$	creep rupture time (h)
1	0.10	0.34	0.55	10.30	2.10	0.12	0.23	3.85	4800
2	0.13	0.32	0.60	9.10	3.20	0.09	0.25	4.05	5090
3	0.11	0.36	0.58	9.75	2.50	0.11	0.24	3.92	4200
4	0.15	0.30	0.70	8.30	1.80	0.10	0.28	4.18	2500

2. **LCF modelling** - The MLP fatigue surrogate exhibits uniformly smooth optimisation behaviour and high predictive accuracy ($R^2 = 0.97$), reflecting the single, well-conditioned cyclic-plasticity mechanism that renders LCF highly learnable across the full life range.
3. **Mechanistic interpretability** - SHAP attribution confirms that both models correctly recover the governing physics: stress-controlled dislocation creep at low T/T_m, diffusion-dominated creep at high T/T_m, and LCF behaviour driven primarily by $\Delta\varepsilon_{total}$, Temperature, and Cr-W-Ta-stabilised microstructures.
4. **Element interactions** - Pairwise SHAP interaction analysis reveals strong cooperative strengthening among Cr-W-Ta under low-temperature creep, a transition to jointly degradation-dominated behaviour at high temperatures, and fatigue resistance governed mainly by Cr-W synergy with minimal Ta influence, reflecting the distinct mechanisms across regimes.
5. **Multi-objective optimisation** - Integration of the PINN and MLP surrogates within NSGA-II yields a clear Pareto frontier that surpasses Eurofer97, identifying alloys with $\log_{10}N_f = 3.85$-4.18 and creep rupture time of 2.5-5.1 $\times 10^3$ h at 650°C, demonstrating that simultaneous enhancement of creep and fatigue performance is achievable within a realistic RAFM compositional space.

Future work will extend the present framework to irradiation environments, where radiation-induced defects, dislocation loops, and irradiation-assisted precipitate evolution can substantially modify creep deformation and cyclic damage mechanisms in RAFM steels. Integrating irradiation parameters together with microstructural descriptors into physics-informed or data-driven models will be essential for improving lifetime prediction and guiding alloy design for fusion reactor structural materials.

CRediT authorship contribution statement

Pengxin Wang: Writing – original draft, Visualization, Validation, Software, Methodology, Investigation, Funding acquisition, Formal analysis, Data curation, Conceptualization. **Yian Lin:** Formal analysis, Data curation. **Mingda Tian:** Formal analysis, Data curation. **G.M.A.M. El-Fallah:** Writing – review & editing, Visualization, Validation, Supervision, Methodology, Investigation, Funding acquisition, Formal analysis, Data curation, Conceptualization.

Declaration of competing interest

The authors declare that they have no known competing financial interests or personal relationships that could have appeared to influence the work reported in this paper.

Acknowledgements

All authors gratefully acknowledge the support from Nanjing Iron & Steel United Co., Ltd. (NISCO), particularly for providing a PhD. scholarship for this study.

Supplementary materials

Supplementary material associated with this article can be found, in the online version, at doi:10.1016/j.jnucmat.2026.156750.

Data availability

Data will be made available on request.

References

[1] S.J. Zinkle, J.T. Busby, Structural materials for fission & fusion energy, Mater. Today 12 (2009) 12–19, https://doi.org/10.1016/S1369-7021(09)70294-9.
[2] L. Tan, L.L. Snead, Y. Katoh, Development of new generation reduced activation ferritic-martensitic steels for advanced fusion reactors, J. Nucl. Mater. 478 (2016) 42–49, https://doi.org/10.1016/j.jnucmat.2016.05.037.
[3] R. Andreani, et al., Overview of the European Union fusion nuclear technologies development and essential elements on the way to DEMO, Fusion Eng. Des. 81 (2006) 25–32, https://doi.org/10.1016/j.fusengdes.2005.09.005.
[4] A. Bhattacharya, et al., Irradiation damage concurrent challenges with RAFM and ODS steels for fusion reactor first-wall/blanket: a review, J. Phys.: Energy 4 (2022) 034003, https://doi.org/10.1088/2515-7655/ac6f7f.
[5] E. Gaganidze, J. Aktaa, Assessment of neutron irradiation effects on RAFM steels, Fusion Eng. Des. 88 (2013) 118–128, https://doi.org/10.1016/j.fusengdes.2012.11.020.
[6] D. Stork, et al., Developing structural, high-heat flux and plasma facing materials for a near-term DEMO fusion power plant: The EU assessment, J. Nucl. Mater. 455 (2014) 277–291, https://doi.org/10.1016/j.jnucmat.2014.06.014.
[7] Y. Zhao, et al., The long-term creep behavior and damage mechanism of RAFM steel for fusion reactors, Fusion Eng. Des. 194 (2023) 113908, https://doi.org/10.1016/j.fusengdes.2023.113908.
[8] J. Aktaa, R. Schmitt, High temperature deformation and damage behavior of RAFM steels under low cycle fatigue loading: Experiments and modeling, Fusion Eng. Des. 81 (2006) 2221–2231, https://doi.org/10.1016/j.fusengdes.2006.03.002.
[9] L. Tan, et al., Recent status and improvement of reduced-activation ferritic-martensitic steels for high-temperature service, J. Nucl. Mater. 479 (2016) 515–523, https://doi.org/10.1016/j.jnucmat.2016.07.054.
[10] G.K. Ahiale, et al., Low-Cycle Fatigue Behavior of Reduced Activation Ferritic-Martensitic Steel at Elevated Temperatures, Met. Mater. Int. 29 (2023) 71–80, https://doi.org/10.1007/s12540-022-01209-5.
[11] S.J. Zinkle, N.M. Ghoniem, Operating temperature windows for fusion reactor structural materials, Fusion Eng. Des. 51-52 (2000) 55–71, https://doi.org/10.1016/S0920-3796(00)00320-3.
[12] V. Shankar, et al., Long term creep-fatigue interaction studies on India-specific reduced activation ferritic-martensitic (IN-RAFM) steel, Int. J. Fatigue 98 (2017) 259–268, https://doi.org/10.1016/j.ijfatigue.2017.01.033.
[13] V. Shankar, et al., Effect of W and Ta on creep–fatigue interaction behavior of reduced activation ferritic–martensitic (RAFM) steels, Fusion Eng. Des. 100 (2015) 314–320, https://doi.org/10.1016/j.fusengdes.2015.06.191.
[14] L. Huang, et al., Laves-phase in the China Low Activation Martensitic steel after long-term creep exposure, Mater. Des. 63 (2014) 333–335, https://doi.org/10.1016/j.matdes.2014.06.028.
[15] R.L. Klueh, Reduced-activation steels: Future development for improved creep strength, J. Nucl. Mater. 378 (2008) 159–166, https://doi.org/10.1016/j.jnucmat.2008.05.010.
[16] H.K. Kim, et al., Effects of Ti and Ta addition on microstructure stability and tensile properties of reduced activation ferritic/martensitic steel for nuclear fusion reactors, J. Nucl. Mater. 500 (2018) 327–336, https://doi.org/10.1016/j.jnucmat.2018.01.008.
[17] C. Mao, et al., Developing of containing Ta, Zr reduced activation ferritic/martensitic (RAFM) steel with excellent creep property, Materials Science and Engineering: A 851 (2022) 143625, https://doi.org/10.1016/j.msea.2022.143625.
[18] Y. Wang, et al., Improving creep properties of RAFM steel with high V & Ta, Int. J. Press. Vessels Pip. 218 (2025) 105581, https://doi.org/10.1016/j.ijpvp.2025.105581.
[19] A. Zinovev, et al., Low cycle fatigue of EUROFER97 investigated for test blanket modules of ITER: An interlaboratory study, J. Nucl. Mater. 597 (2024) 155127, https://doi.org/10.1016/j.jnucmat.2024.155127.
[20] K. Laha, et al., Development of India-specific RAFM steel through optimization of tungsten and tantalum contents for better combination of impact, tensile, low cycle fatigue and creep properties, J. Nucl. Mater. 439 (2013) 41–50, https://doi.org/10.1016/j.jnucmat.2013.03.073.
[21] H. Tanigawa, et al., Status and key issues of reduced activation ferritic/martensitic steels as the structural material for a DEMO blanket, J. Nucl. Mater. 417 (2011) 9–15, https://doi.org/10.1016/j.jnucmat.2011.05.023.

[22] N. Luptáková, et al., The Irradiation Effects in Ferritic, Ferritic–Martensitic and Austenitic Oxide Dispersion Strengthened Alloys: A Review, Materials 17 (2024) 3409. https://10.3390/ma17143409.
[23] G.S. Was, Fundamentals of radiation materials science: metals and alloys, Springer, 2007.
[24] Q. Yuan, et al., Dislocation loop coarsening and shape evolution upon annealing neutron-irradiated RAFM steel, J. Nucl. Mater. 558 (2022) 153366, https://doi.org/10.1016/j.jnucmat.2021.153366.
[25] T.M.K. Green, et al., MX precipitate behavior in an irradiated advanced Fe-9Cr steel: Helium effects on phase stability, Acta Mater 296 (2025) 121202, https://doi.org/10.1016/j.actamat.2025.121202.
[26] S. Kano, et al., Study of radiation-induced amorphization of M23C6 in RAFM steels under iron irradiations, J. Nucl. Mater. 533 (2020) 152088, https://doi.org/10.1016/j.jnucmat.2020.152088.
[27] S. Kim, et al., Irradiation hardening and mechanical behavior of K-RAFM steels subjected to Fe ion irradiation at doses up to 20 dpa, Fusion Eng. Des. 218 (2025) 115235, https://doi.org/10.1016/j.fusengdes.2025.115235.
[28] E. Gaganidze, et al., Mechanical properties and TEM examination of RAFM steels irradiated up to 70dpa in BOR-60, J. Nucl. Mater. 417 (2011) 93–98, https://doi.org/10.1016/j.jnucmat.2010.12.047.
[29] A. Sarkar, V.D. Vijayanand, R. Sandhya, Generation of creep-fatigue interaction diagram for an indigenous reduced activation ferritic martensitic steel (INRAFMS) at 823 K based on sequential tests, Fusion Eng. Des. 138 (2019) 27–31, https://doi.org/10.1016/j.fusengdes.2018.10.028.
[30] B. Fournier, et al., High temperature creep–fatigue–oxidation interactions in 9–12%Cr martensitic steels, J. Nucl. Mater. 386-388 (2009) 418–421, https://doi.org/10.1016/j.jnucmat.2008.12.139.
[31] M. Speicher, D. Jobski, C. Kontermann, Creep-Fatigue Interactions in 9CR Martensitic Cast Steel—Microstructure and Mechanical Behavior, AM-EPRI, 2019.
[32] P. Wang, et al., Advanced machine learning analysis of radiation hardening in reduced-activation ferritic/martensitic steels, Comput. Mater. Sci 251 (2025) 113773, https://doi.org/10.1016/j.commatsci.2025.113773.
[33] C. Shen, et al., Physical metallurgy-guided machine learning and artificial intelligent design of ultrahigh-strength stainless steel, Acta Mater 179 (2019) 201–214, https://doi.org/10.1016/j.actamat.2019.08.033.
[34] C. Yang, et al., A machine learning-based alloy design system to facilitate the rational design of high entropy alloys with enhanced hardness, Acta Mater 222 (2022) 117431, https://doi.org/10.1016/j.actamat.2021.117431.
[35] G.L.W. Hart, et al., Machine learning for alloys, Nat. Rev. Mater. 6 (2021) 730–755, https://doi.org/10.1038/s41578-021-00340-w.
[36] G. Pilania, Machine learning in materials science: From explainable predictions to autonomous design, Comput. Mater. Sci 193 (2021) 110360, https://doi.org/10.1016/j.commatsci.2021.110360.
[37] X. Liu, et al., Material machine learning for alloys: Applications, challenges and perspectives, J. Alloys Compd. 921 (2022) 165984, https://doi.org/10.1016/j.jallcom.2022.165984.
[38] Y. Diao, L. Yan, K. Gao, A strategy assisted machine learning to process multi-objective optimization for improving mechanical properties of carbon steels, Journal of Materials Science & Technology 109 (2022) 86–93, https://doi.org/10.1016/j.jmst.2021.09.004.
[39] P. Zhang, Y. Qian, Q. Qian, Multi-objective optimization for materials design with improved NSGA-II, Mater. Today Commun. 28 (2021) 102709, https://doi.org/10.1016/j.mtcomm.2021.102709.
[40] P. Wang, G.M.A.M. El-Fallah, A Data-driven machine learning model for radiation-induced DBTT shifts in RAFM steels, J. Nucl. Mater. 615 (2025) 155984, https://doi.org/10.1016/j.jnucmat.2025.155984.
[41] G.P.P. Pun, et al., Physically informed artificial neural networks for atomistic modeling of materials, Nat. Commun. 10 (2019) 2339, https://doi.org/10.1038/s41467-019-10343-5.
[42] P. Wang, G.M.A.M. El-Fallah, Physically- and Knowledge-Informed deep learning for robust prediction of martensite start temperature in steels, Mater. Today Commun. 49 (2025) 113743, https://doi.org/10.1016/j.mtcomm.2025.113743.
[43] G.E. Karniadakis, et al., Physics-informed machine learning, Nat. Rev. Phys. 3 (2021) 422–440, https://doi.org/10.1038/s42254-021-00314-5.
[44] M. Raissi, P. Perdikaris, G.E. Karniadakis, Physics-informed neural networks: A deep learning framework for solving forward and inverse problems involving nonlinear partial differential equations, J. Comput. Phys. 378 (2019) 686–707, https://doi.org/10.1016/j.jcp.2018.10.045.
[45] V. Igwemezie, et al., Review of Physical Metallurgy of Creep Steel for the Design of Modern Steam Power Plants-Fundamental Theories and Parametric Models, Journal of Engineering Science & Technology Review 8 (2015), https://doi.org/10.25103/jestr.085.12.
[46] T.G. Langdon, F.A. Mohamed, A new type of deformation mechanism map for high-temperature creep, Materials Science and Engineering 32 (1978) 103–112, https://doi.org/10.1016/0025-5416(78)90029-0.
[47] Y. LeCun, Y. Bengio, G. Hinton, Deep learning, nature 521 (2015) 436–444, https://doi.org/10.1038/nature14539.
[48] K. Hornik, M. Stinchcombe, H. White, Multilayer feedforward networks are universal approximators, Neural Networks 2 (1989) 359–366, https://doi.org/10.1016/0893-6080(89)90020-8.
[49] P. Marmy, T. Kruml, Low cycle fatigue of Eurofer 97, J. Nucl. Mater. 377 (2008) 52–58, https://doi.org/10.1016/j.jnucmat.2008.02.054.
[50] L. Breiman, Random Forests, Machine Learning 45 (2001) 5–32, https://doi.org/10.1023/A:1010933404324.
[51] T. Hastie, et al., The elements of statistical learning: data mining, inference, and prediction, Springer, 2009.
[52] J.H. Friedman, Greedy Function Approximation: A Gradient Boosting Machine, The Annals of Statistics 29 (2001) 1189–1232. http://www.jstor.org/stable/2699986.
[53] T. Chen, C. Guestrin, XGBoost: A Scalable Tree Boosting System, in: Proceedings of the 22nd ACM SIGKDD International Conference on Knowledge Discovery and Data Mining, Association for Computing Machinery, San Francisco, California, USA, 2016, pp. 785–794.
[54] T.-Y. Kim, et al., Influence of Ti addition on MX precipitation and creep-fatigue properties of RAFM steel for nuclear fusion reactor, J. Nucl. Mater. 571 (2022) 154001, https://doi.org/10.1016/j.jnucmat.2022.154001.
[55] G. Yu, N. Nita, N. Baluc, Thermal creep behaviour of the EUROFER 97 RAFM steel and two European ODS EUROFER 97 steels, Fusion Eng. Des. 75-79 (2005) 1037–1041, https://doi.org/10.1016/j.fusengdes.2005.06.311.
[56] C. Cristalli, et al., Mechanical properties of several newly produced RAFM steels with Tungsten content in the range of 2 wt%, Nucl. Mater. Energy 25 (2020) 100793 https://doi.org/10.1016/j.nme.2020.100793.
[57] M.D. Mathew, et al., Tensile and creep properties of reduced activation ferritic–martensitic steel for fusion energy application, J. Nucl. Mater. 417 (2011) 77–80, https://doi.org/10.1016/j.jnucmat.2011.01.058.
[58] J. Vanaja, et al., Creep deformation and rupture behaviour of 9Cr–1W–0.2V–0.06Ta Reduced Activation Ferritic–Martensitic steel, Materials Science and Engineering: A 533 (2012) 17–25, https://doi.org/10.1016/j.msea.2011.10.112.
[59] Y.B. Chun, et al., Improvement of creep and impact resistance of reduced activation ferritic–martensitic steel by the addition of Zr, Materials Science and Engineering: A 645 (2015) 286–291, https://doi.org/10.1016/j.msea.2015.08.033.
[60] L. Liu, et al., Research on thermal creep behavior of Chinese low-activation ferritic/martensitic steel, Fusion Eng. Des. 194 (2023) 113897, https://doi.org/10.1016/j.fusengdes.2023.113897.
[61] R. Lindau, A. Möslang, M. Schirra, Thermal and mechanical behaviour of the reduced-activation-ferritic-martensitic steel EUROFER, Fusion Eng. Des. 61-62 (2002) 659–664, https://doi.org/10.1016/S0920-3796(02)00178-3.
[62] P. Fernández, et al., Creep strength of reduced activation ferritic/martensitic steel Eurofer'97, Fusion Eng. Des. 75-79 (2005) 1003–1008, https://doi.org/10.1016/j.fusengdes.2005.06.085.
[63] Y. de Carlan, et al., Design of new Fe–9CrWV reduced-activation martensitic steels for creep properties at 650°C, J. Nucl. Mater. 329-333 (2004) 238–242, https://doi.org/10.1016/j.jnucmat.2004.04.017.
[64] H. Kayano, et al., Effects of small changes in alloy composition on the mechanical properties of low activation 9%Cr-2%W steel, J. Nucl. Mater. 179-181 (1991) 671–674, https://doi.org/10.1016/0022-3115(91)90178-A.
[65] C.K.E. Association, et al., The mechanical behaviour of newly designed low-activation high-chromium martensitic steels, J. Nucl. Mater. 179-181 (1991) 659–662, https://doi.org/10.1016/0022-3115(91)90175-7.
[66] K.W. Tupholme, D. Dulieu, G.J. Butterworth, The development of low-activation martensitic 9 and 11%Cr,W,V stainless steels for fusion reactor applications, J. Nucl. Mater. 155-157 (1988) 650–655, https://doi.org/10.1016/0022-3115(88)90389-3.
[67] K. Wang, et al., Effect of Tantalum Content on Creep Properties of CLAM Steel, J. Fusion Energy 35 (2016) 193–198, https://doi.org/10.1007/s10894-015-9989-1.
[68] A.A.F. Tavassoli, et al., Materials design data for reduced activation martensitic steel type F82H, Fusion Eng. Des. 61-62 (2002) 617–628, https://doi.org/10.1016/S0920-3796(02)00255-7.
[69] R.L. Klueh, R.W. Swindeman, The microstructure and mechanical properties of a modified 2.25Cr-lMo steel, Metall. Trans. A 17 (1986) 1027–1034, https://doi.org/10.1007/BF02661268.
[70] R.L. Klueh, Heat treatment effects on creep and rupture behavior of annealed 2.25 Cr-1 Mo steel, Metall. Trans. A 9 (1978) 1591–1598, https://doi.org/10.1007/BF02661941.
[71] R.L. Klueh, J.L. Griffith, Mechanical properties of a 2-1/4 Cr-1 Mo steel tubesheet forging, J. Mater. Energy Syst. 3 (1981) 26–38, https://doi.org/10.1007/BF02833318.
[72] R.L. Klueh, Heat Treatment of Cr—1 Mo Steel for Breeder Reactor Steam Generators, Nucl. Technol. 57 (1982) 114–124, https://doi.org/10.13182/NT82-A16191.
[73] F. Abe, et al., Alloy composition selection for improving strength and toughness of reduced activation 9Cr-W steels, J. Nucl. Mater. 179-181 (1991) 663–666, https://doi.org/10.1016/0022-3115(91)90176-8.
[74] K. Ehrlich, et al., The development of ferritic-martensitic steels with reduced long-term activation, J. Nucl. Mater. 212-215 (1994) 678–683, https://doi.org/10.1016/0022-3115(94)90144-9.
[75] V.C. Igwemezie, C.C. Ugwuegbu, U. Mark, Physical Metallurgy of Modern Creep-Resistant Steel for Steam Power Plants: Microstructure and Phase Transformations, Journal of Metallurgy 2016 (2016) 5468292, https://doi.org/10.1155/2016/5468292.
[76] R.O. Kaybyshev, V.N. Skorobogatykh, I.A. Shchenkova, New martensitic steels for fossil power plant: Creep resistance, The Physics of Metals and Metallography 109 (2010) 186–200, https://doi.org/10.1134/S0031918X10020110.
[77] J.D. Robson, H.K.D.H. Bhadeshia, Modelling precipitation sequences in powerplant steels Part 2 – Application of kinetic theory, Mater. Sci. Technol. 13 (1997) 640–644, https://doi.org/10.1179/mst.1997.13.8.640.

[78] K. Miyata, Y. Sawaragi, Effect of Mo and W on the Phase Stability of Precipitates in Low Cr Heat Resistant Steels, ISIJ Int 41 (2001) 281–289, https://doi.org/10.2355/isijinternational.41.281.
[79] B.G.M.A.M. El-Fallah, K.D.H. H, Tensile behaviour of thermally-stable nanocrystalline bainitic-steels, Materials Science and Engineering: A 746 (2019) 145–153, https://doi.org/10.1016/j.msea.2018.12.124.
[80] G.M.A.M. El-Fallah, S.W. Ooi, H.K.D.H. Bhadeshia, Effect of nickel aluminide on the bainite transformation in a Fe-0.45C–13Ni–3Al–4Co steel, and associated properties, Materials Science and Engineering: A 767 (2019) 138362, https://doi.org/10.1016/j.msea.2019.138362.
[81] G.M.A.M. El-Fallah, Dilatometric study of high silicon bainitic steels: Solid-state transformations, Results Mater 19 (2023) 100430, https://doi.org/10.1016/j.rinma.2023.100430.
[82] G.M.A.M. El-Fallah, Structural evolution during the plastic deformation of nanostructured steel. PhD thesis, University of Cambridge, 2019.
[83] A. Raj, B. Goswami, A.K. Ray, Creep and Fatigue Behavior in Micro-alloyed Steels-A Review, High Temperature Materials & Processes 33 (2014), https://doi.org/10.1515/htmp-2012-0177.
[84] Y.-X. Guo, et al., Correlations between valence electron concentration and the phase stability, intrinsic strength, and deformation mechanism in fcc multicomponent alloys, Physical Review B 109 (2024) 024102, https://doi.org/10.1103/PhysRevB.109.024102.
[85] P.I. Odetola, et al., Exploring high entropy alloys: A review on thermodynamic design and computational modeling strategies for advanced materials applications, Heliyon 10 (2024), https://doi.org/10.1016/j.heliyon.2024.e39660.
[86] W. Cheng, F. Yuan, X. Wu, Coupled Strengthening Effects by Lattice Distortion, Local Chemical Ordering, and Nanoprecipitates in Medium-Entropy Alloys, Frontiers in Materials 8 (2021), https://doi.org/10.3389/fmats.2021.767795, 2021.
[87] R. Sandström, Creep with Low Stress Exponents, in: R. Sandström (Ed.), Basic Modeling and Theory of Creep of Metallic Materials, Springer Nature Switzerland, Cham, 2024, pp. 83–114.
[88] M. Čanađija, Creep and thermoviscoplasticity of metals, in: M. Čanađija (Ed.), Thermomechanics of Solids and Structure, Elsevier, 2023, pp. 233–261, s.
[89] A. Takeuchi, A. Inoue, Calculations of Mixing Enthalpy and Mismatch Entropy for Ternary Amorphous Alloys, Mater. Trans., JIM 41 (2000) 1372–1378, https://doi.org/10.2320/matertrans1989.41.1372.
[90] A. Vaswani, et al., Attention is all you need. Advances in neural information processing systems, 2017, p. 30, https://doi.org/10.48550/arXiv.1706.03762.
[91] F.H. Norton, The creep of steel at high temperatures, McGraw-Hill Book Company, Incorporated, 1929.
[92] K. Mariappan, et al., Low cycle fatigue design data for India-specific reduced activation ferritic-martensitic (IN-RAFM) steel, Fusion Eng. Des. 104 (2016) 76–83, https://doi.org/10.1016/j.fusengdes.2016.02.021.
[93] M. Roldán, et al., Deformation behaviour and microstructural evolution of EUROFER97-2 under low cycle fatigue conditions, Mater. Charact. 158 (2019) 109943, https://doi.org/10.1016/j.matchar.2019.109943.
[94] T. Hirose, et al., Evaluation of fatigue properties of reduced activation ferritic/martensitic steel, F82H for development of design criteria, Fusion Eng. Des. 160 (2020) 111823, https://doi.org/10.1016/j.fusengdes.2020.111823.
[95] T. Hirose, et al., Effects of test environment on high temperature fatigue properties of reduced activation ferritic/martensitic steel, F82H, Fusion Eng. Des. 136 (2018) 1073–1076, https://doi.org/10.1016/j.fusengdes.2018.04.072.
[96] X. Hu, et al., Low cycle fatigue properties of CLAM steel at room temperature, Fusion Eng. Des. 88 (2013) 3050–3059, https://doi.org/10.1016/j.fusengdes.2013.08.001.
[97] Y. Zhao, X. Zhai, S. Liu, Low cycle fatigue properties of CLAM steel at 450°C and 550°C, Fusion Eng. Des. 112 (2016) 213–217, https://doi.org/10.1016/j.fusengdes.2016.08.015.
[98] A. Nishimura, et al., Low cycle fatigue properties of a low activation ferritic steel (JLF-1) at room temperature, J. Nucl. Mater. 283-287 (2000) 677–680, https://doi.org/10.1016/S0022-3115(00)00112-4.
[99] V. Shankar, et al., Effect of tungsten and tantalum on the low cycle fatigue behavior of reduced activation ferritic/martensitic steels, Fusion Eng. Des. 87 (2012) 318–324, https://doi.org/10.1016/j.fusengdes.2012.01.020.
[100] X. Zhai, et al., Effect of Tantalum content on the low cycle fatigue properties of CLAM steel at 823K, Fusion Eng. Des. 114 (2017) 211–218, https://doi.org/10.1016/j.fusengdes.2016.11.018.
[101] K. Guguloth, et al., Low-cyclic fatigue behavior of modified 9Cr–1Mo steel at elevated temperature, Materials Science and Engineering: A 604 (2014) 196–206, https://doi.org/10.1016/j.msea.2014.02.076.
[102] P. Verma, et al., Low cycle fatigue behavior of modified 9Cr–1Mo steel at room temperature, Materials Science and Engineering: A 652 (2016) 30–41, https://doi.org/10.1016/j.msea.2015.11.060.
[103] B. Fournier, et al., Comparison of various 9–12%Cr steels under fatigue and creep-fatigue loadings at high temperature, Materials Science and Engineering: A 528 (2011) 6934–6945, https://doi.org/10.1016/j.msea.2011.05.046.
[104] Q. Wang, et al., A comparative study of low cycle fatigue behavior and microstructure of Cr-based steel at room and high temperatures, Mater. Des. 195 (2020) 109000, https://doi.org/10.1016/j.matdes.2020.109000.
[105] J.S. Park, S.J. Kim, C.S. Lee, Effect of W addition on the low cycle fatigue behavior of high Cr ferritic steels, Materials Science and Engineering: A 298 (2001) 127–136, https://doi.org/10.1016/S0921-5093(00)01291-0.
[106] X.Y. Long, F.C. Zhang, C.Y. Zhang, Effect of Mn content on low-cycle fatigue behaviors of low-carbon bainitic steel, Materials Science and Engineering: A 697 (2017) 111–118, https://doi.org/10.1016/j.msea.2017.04.089.
[107] J. Kang, et al., Low cycle fatigue behavior in a medium-carbon carbide-free bainitic steel, Materials Science and Engineering: A 666 (2016) 88–93, https://doi.org/10.1016/j.msea.2016.03.077.
[108] H.J. Frost, M.F. Ashby, Deformation-mechanism maps: the plasticity and creep of metals and ceramics, 1982.
[109] R.W. Evans, B. Wilshire, Creep of metals and alloys, 1985.
[110] M.E. Kassner, Chapter 1 - Fundamentals of Creep in Materials, in: M.E. Kassner (Ed.), Fundamentals of Creep in Metals and Alloys, Third Edition, Butterworth-Heinemann, Boston, 2015, pp. 1–6.
[111] E. Ma, X. Wu, Tailoring heterogeneities in high-entropy alloys to promote strength–ductility synergy, Nat. Commun. 10 (2019) 5623, https://doi.org/10.1038/s41467-019-13311-1.
[112] J.W. Yeh, et al., Nanostructured High-Entropy Alloys with Multiple Principal Elements: Novel Alloy Design Concepts and Outcomes, Adv. Eng. Mater. 6 (2004) 299–303, https://doi.org/10.1002/adem.200300567.
[113] D.B. Miracle, O.N. Senkov, A critical review of high entropy alloys and related concepts, Acta Mater 122 (2017) 448–511, https://doi.org/10.1016/j.actamat.2016.08.081.
[114] P.H.F. Oliveira, et al., Exploring the relative influence of atomic parameters on solid solution strengthening, Nat. Commun. 16 (2025) 8865, https://doi.org/10.1038/s41467-025-63900-6.
[115] P. Thirathipviwat, et al., A role of atomic size misfit in lattice distortion and solid solution strengthening of TiNbHfTaZr high entropy alloy system, Scr. Mater. 210 (2022) 114470, https://doi.org/10.1016/j.scriptamat.2021.114470.
[116] V. B, M. A.X, Development of high entropy alloys (HEAs): Current trends, Heliyon 10 (2024) e26464, https://doi.org/10.1016/j.heliyon.2024.e26464.
[117] K. Maruyama, K. Sawada, J.-i. Koike, Strengthening Mechanisms of Creep Resistant Tempered Martensitic Steel, ISIJ Int 41 (2001) 641–653, https://doi.org/10.2355/isijinternational.41.641.
[118] F. Abe, Creep rates and strengthening mechanisms in tungsten-strengthened 9Cr steels, Materials Science and Engineering: A 319-321 (2001) 770–773, https://doi.org/10.1016/S0921-5093(00)02002-5.
[119] L. Tan, W. Zhong, T. Chen, Microstructural stability of tantalum-alloyed ferritic-martensitic steel with neutron irradiation to 7.4 dpa at ~490°C, Materialia 9 (2020) 100608, https://doi.org/10.1016/j.mtla.2020.100608.
[120] W. Blum, P. Eisenlohr, F. Breutinger, Understanding creep—a review, Metallurgical and Materials Transactions A 33 (2002) 291–303, https://doi.org/10.1007/s11661-002-0090-9.
[121] R. Sandström, Basic modeling and theory of creep of metallic materials, Springer Nature, 2024.
[122] T.G. Langdon, Review: developments in the creep of materials over a period of more than a century, J. Mater. Sci. 60 (2025) 18158–18176, https://doi.org/10.1007/s10853-025-10922-6.
[123] T. Breithaupt, et al., Dislocation theory of steady and transient creep of crystalline solids: Predictions for olivine, Proc Natl Acad Sci U S A 120 (2023) e2203448120, https://doi.org/10.1073/pnas.2203448120.
[124] R.N. Stevens, Grain boundary sliding and diffusion creep, Surf. Sci. 31 (1972) 543–565, https://doi.org/10.1016/0039-6028(72)90274-9.
[125] S.D. Mesarovic, Lattice continuum and diffusional creep, Proceedings of the Royal Society A: Mathematical, Physical and Engineering Sciences 472 (2016) 20160039, https://doi.org/10.1098/rspa.2016.0039.
[126] A. Seoane, D. Farkas, X.-M. Bai, Influence of compositional complexity on species diffusion behavior in high-entropy solid-solution alloys, J. Mater. Res. 37 (2022) 1403–1415, https://doi.org/10.1557/s43578-022-00545-x.
[127] X. Zhang, et al., Effects of lattice distortion and chemical short-range ordering on the incipient behavior of Ti-based multi-principal element alloys: MD simulations and DFT calculations, Int. J. Plast. 166 (2023) 103643, https://doi.org/10.1016/j.ijplas.2023.103643.
[128] F.X. Zhang, H.-Q. Song, Effect of atomic size mismatch and chemical complexity on the local lattice distortion of BCC solid solution alloys, Mater. Today Commun. 33 (2022) 104367, https://doi.org/10.1016/j.mtcomm.2022.104367.
[129] M. Godec, D.A. Skobir Balantič, Coarsening behaviour of M23C6 carbides in creep-resistant steel exposed to high temperatures, Sci. Rep. 6 (2016) 29734, https://doi.org/10.1038/srep29734.
[130] O. Prat, et al., Investigations on coarsening of MX and M23C6 precipitates in 12% Cr creep resistant steels assisted by computational thermodynamics, Materials Science and Engineering: A 527 (2010) 5976–5983, https://doi.org/10.1016/j.msea.2010.05.084.
[131] J.-h. Zhou, Y.-f. Shen, N. Jia, Strengthening mechanisms of reduced activation ferritic/martensitic steels: A review, International Journal of Minerals, Metallurgy and Materials 28 (2021) 335–348, https://doi.org/10.1007/s12613-020-2121-1.
[132] R. Goodall, et al., Development of a boron-containing reduced activation Ferritic-Martensitic (B-RAFM) steel, Ironmaking & Steelmaking 52 (2024) 660–671, https://doi.org/10.1177/03019233241273484.
[133] R.L. Klueh, Ferritic/martensitic steels for advanced nuclear reactors, Trans. Indian Inst. Met. 62 (2009) 81–87, https://doi.org/10.1007/s12666-009-0011-3.
[134] T. Nakazawa, et al., Advanced type stainless steel 316FR for fast breeder reactor structures, J. Mater. Process. Technol. 143-144 (2003) 905–909, https://doi.org/10.1016/S0924-0136(03)00484-9.
[135] W.-G. Kim, S.-H. Kim, W.-S. Ryu, Creep characterization of type 316LN and HT-9 stainless steels by the K-R creep damage model, KSME International Journal 15 (2001) 1463–1471, https://doi.org/10.1007/BF03185735.

[136] S. Holmström, et al., Creep and Creep-fatigue Behaviour of 316 Stainless Steel, Procedia Eng 55 (2013) 160–164, https://doi.org/10.1016/j.proeng.2013.03.236.
[137] L.F. Coffin Jr., A Study of the Effects of Cyclic Thermal Stresses on a Ductile Metal, Transactions of the American Society of Mechanical Engineers 76 (2022) 931–949, https://doi.org/10.1115/1.4015020.
[138] S.S. Manson, Behavior of materials under conditions of thermal stress. National Advisory Committee for Aeronautics, 1953.
[139] R.I. Stephens, et al., Metal Fatigue in Engineering, Wiley, 2000.
[140] M. Sauzay, et al., Cyclic softening of martensitic steels at high temperature—Experiments and physically based modelling, Materials Science and Engineering: A 483-484 (2008) 410–414, https://doi.org/10.1016/j.msea.2006.12.183.
[141] S. Goyal, et al., Assessment of fatigue response of thermally aged reduced activation ferritic-martensitic steel based on finite element analysis, Mater. High Temp. 33 (2016) 170–178, https://doi.org/10.1179/1878641315Y.0000000020.
[142] G.-x. Qiu, et al., Review on development of reduced activated ferritic/martensitic steel for fusion reactor, J. Iron. Steel Res. Int. 29 (2022) 1343–1356, https://doi.org/10.1007/s42243-022-00796-2.
[143] S.-Y. Jun, et al., Atomic scale identification of nano-sized precipitates of Ta/Ti-added RAFM steel and its superior creep strength, Mater. Charact. 169 (2020) 110596, https://doi.org/10.1016/j.matchar.2020.110596.
[144] Q. Gao, et al., Precipitates and Particles Coarsening of 9Cr–1.7W–0.4Mo–Co Ferritic Heat-Resistant Steel after Isothermal Aging, Sci. Rep. 7 (2017) 5859, https://doi.org/10.1038/s41598-017-06191-2.
[145] Y.Z. Shen, et al., TEM investigations of MN nitride phases in a 9% chromium ferritic/martensitic steel with normalization conditions for nuclear reactors, J. Nucl. Mater. 384 (2009) 48–55, https://doi.org/10.1016/j.jnucmat.2008.10.005.
[146] G. Golański, et al., Quantitative analysis of stability of 9% Cr steel microstructure after long-term ageing, Arch. Metall. Mater. 62 (2017) 263–271, https://doi.org/10.1515/amm-2017-0040.
[147] Z. Zhang, et al., Experimental and numerical investigation of low-cycle fatigue behavior of 9Cr ferritic-martensitic steel at room temperature, Mater. Des. Process. Commun. 2 (2020) e130, https://doi.org/10.1002/mdp2.130.
[148] M. Jürgens, et al., Low Cycle Fatigue and Relaxation Performance of Ferritic–Martensitic Grade P92 Steel, Metals 9 (2019) 99, https://doi.org/10.3390/met9010099.
[149] G.J. Butterworth, P. Komarek, Low activation structural materials for fusion, Fusion Eng. Des. 11 (1989) 231–244, https://doi.org/10.1016/B978-0-444-87369-9.50025-1.
[150] T. Noda, et al., Materials selection for reduced activation of fusion reactors, J. Nucl. Mater. 155-157 (1988) 581–584, https://doi.org/10.1016/0022-3115(88)90375-3.
[151] H.J. Chang, J.J. Kai, Effects of temperature on the low cycle fatigue and microstructures of HT-9 ferritic steel, J. Nucl. Mater. 191-194 (1992) 836–840, https://doi.org/10.1016/0022-3115(92)90590-H.
[152] C. Han-Jou, K. Ji-Jung, T. Chuen-Horng, Cyclic deformation property and microstructure study of HT-9 ferritic steel at elevated temperatures, J. Nucl. Mater. 212-215 (1994) 574–578, https://doi.org/10.1016/0022-3115(94)90125-2.
[153] R. Hormozi, F. Biglari, K. Nikbin, Experimental and numerical creep–fatigue study of Type 316 stainless steel failure under high temperature LCF loading condition with different hold time, Eng. Fract. Mech. 141 (2015) 19–43, https://doi.org/10.1016/j.engfracmech.2015.05.007.
[154] P. Yin, et al., Dynamic strain aging and microstructural damage mechanism of austenitic stainless steel under thermomechanical fatigue in the temperature range of 250–400°C, Int. J. Fatigue 163 (2022) 107111, https://doi.org/10.1016/j.ijfatigue.2022.107111.
[155] A. Fedoseeva, et al., Effect of Tungsten on Creep Behavior of 9%Cr–3%Co Martensitic Steels, Metals 7 (2017) 573, https://doi.org/10.3390/met7120573.
[156] S.G. Hong, W.B. Lee, C.G. Park, The effects of tungsten addition on the microstructural stability of 9Cr–Mo Steels, J. Nucl. Mater. 288 (2001) 202–207, https://doi.org/10.1016/S0022-3115(00)00558-4.
[157] L. Ma, Y. Wang, G. Di, Study on the Microstructure Evolution and Tungsten Content Optimization of 9Cr-3W-3Co Steel, Materials (Basel) 11 (2018), https://doi.org/10.3390/ma11112080.
[158] Z. Yang, et al., Dissolution of M23C6 and New Phase Re-Precipitation in Fe Ion-Irradiated RAFM Steel, Metals 8 (2018) 349, https://doi.org/10.3390/met8050349.
[159] T. Nagasaka, et al., Analysis on precipitation behavior of reduced activation ferritic/martensitic steels with extraction residue tests, Fusion Eng. Des. 88 (2013) 2565–2568, https://doi.org/10.1016/j.fusengdes.2013.05.037.
[160] A. Puype, et al., Effect of W and N on mechanical properties of reduced activation ferritic/martensitic EUROFER-based steel grades, J. Nucl. Mater. 502 (2018) 282–288, https://doi.org/10.1016/j.jnucmat.2018.02.017.
[161] J. Chen, et al., Improvement of High-Temperature Mechanical Properties of Low-Carbon RAFM Steel by MX Precipitates, Acta Metallurgica Sinica (English Letters) 31 (2018) 706–712, https://doi.org/10.1007/s40195-018-0703-y.
[162] X. Xiao, et al., Effect of V and Ta on the precipitation behavior of 12% Cr reduced activation ferrite/martensite steel, Mater. Charact. 82 (2013) 130–139, https://doi.org/10.1016/j.matchar.2013.05.006.
[163] C. Wang, et al., Design of Reduced Activation Ferritic/Martensitic Steels by Multiphase Optimization during the Entire Processing, ISIJ Int 59 (2019) 1715–1722, https://doi.org/10.2355/isijinternational.ISIJINT-2019-143.
[164] F. Abe, Effect of fine precipitation and subsequent coarsening of Fe2W laves phase on the creep deformation behavior of tempered martensitic 9Cr-W steels, Metallurgical and Materials Transactions A 36 (2005) 321–332, https://doi.org/10.1007/s11661-005-0305-y.
[165] V.Thomas Paul, et al., Effect of Tungsten on Long-Term Microstructural Evolution and Impression Creep Behavior of 9Cr Reduced Activation Ferritic/Martensitic Steel, Metallurgical and Materials Transactions A 48 (2017) 425–438, https://doi.org/10.1007/s11661-016-3823-x.
[166] L. Tan, Y. Katoh, L.L. Snead, Stability of the strengthening nanoprecipitates in reduced activation ferritic steels under Fe2+ ion irradiation, J. Nucl. Mater. 445 (2014) 104–110, https://doi.org/10.1016/j.jnucmat.2013.11.003.
[167] Y. Shen, et al., Identification of tantalum precipitates in CLAM steel, J. Nucl. Mater. 549 (2021) 152856, https://doi.org/10.1016/j.jnucmat.2021.152856.
[168] L. Yang, F. Zhao, W. Ding, Laves phase evolution in China low-activation martensitic (CLAM) steel during long-term aging at 550°C, Materials 13 (2019) 154, https://doi.org/10.3390/ma13010154.
[169] J.-G. Chen, et al., Effects of Isothermal Aging on Microstructure and Mechanical Property of Low-Carbon RAFM Steel, Acta Metallurgica Sinica (English Letters) 32 (2019) 1151–1160, https://doi.org/10.1007/s40195-019-00883-6.
[170] F. Abe, Precipitate design for creep strengthening of 9% Cr tempered martensitic steel for ultra-supercritical power plants, Sci. Technol. Adv. Mater. 9 (2008) 013002, https://doi.org/10.1088/1468-6996/9/1/013002.
[171] F. Abe, H. Araki, T. Noda, The effect of tungsten on dislocation recovery and precipitation behavior of low-activation martensitic 9Cr steels, Metall. Trans. A 22 (1991) 2225–2235, https://doi.org/10.1007/BF02664988.
[172] X. Hu, et al., Microstructure evolution in CLAM steel under low cycle fatigue, Materials Science and Engineering: A 607 (2014) 356–359, https://doi.org/10.1016/j.msea.2014.04.005.
[173] R. Lindau, et al., Present development status of EUROFER and ODS-EUROFER for application in blanket concepts, Fusion Eng. Des. 75-79 (2005) 989–996, https://doi.org/10.1016/j.fusengdes.2005.06.186.
[174] M. Klimenkov, R. Lindau, A. Möslang, New insights into the structure of ODS particles in the ODS-Eurofer alloy, J. Nucl. Mater. 386-388 (2009) 553–556, https://doi.org/10.1016/j.jnucmat.2008.12.174.
[175] R. Klueh, D. Harries, High-Chromium Ferritic and Martensitic Steels for Nuclear Applications, ASTM International, 2001.
[176] G. Krauss, Steels: Processing, Structure, and Performance, ASM International, 2015.
[177] K. Ding, et al., Low cycle fatigue and creep-fatigue interaction behavior of C630R ferritic/martensitic heat-resistant steel at high temperature, Int. J. Fatigue 194 (2025) 108836, https://doi.org/10.1016/j.ijfatigue.2025.108836.